Project Acronym:

SOUNDPET (INTEGRATED/0918/0008)

MRI-guided Focused ultraSOUND system for cancer in PETs (dogs and cats)

Deliverable number: 2.3

Title: Publication in a scientific journal

Prepared by:

Marinos Giannakou (MEDSONIC, Limassol, Cyprus)
Theocharis Drakos (MEDSONIC, Limassol, Cyprus)
Nikolas Evripidou (CUT, Limassol, Cyprus)
Anastasia Antoniou (CUT, Limassol, Cyprus)
Christakis Damianou (CUT, Limassol, Cyprus)
Georgios Constantinides (CUT, Limassol, Cyprus)
Leonidas Georgiou (GOC, Limassol, Cyprus)
Theodora Christodoulou (GOC, Limassol, Cyprus)
Natalie Panayiotou (GOC, Limassol, Cyprus)
Cleanthis Ioannides (GOC, Limassol, Cyprus)
Nikolaos Zamboglou (GOC, Limassol, Cyprus)

Date: 14/11/2021

Ευρωπαϊκή Ένωση
Ευρωπαϊκά Διαρθρωτικά και Επενδυτικά Ταμεία
Κυπριακή Δημοκρατία
Διαρθρωτικά Ταμεία της Ευρωπαϊκής Ένωσης στην Κύπρο

Table of Contents

Executive summary

This deliverable presents the Journal papers that were published during the first year of the SOUNDPET project. A scientific paper entitiled “Characterization of a soft tissue-mimicking agar/wood powder material for MRgFUS application” was published in the *Journal of Ultrasonics* (Accepted: January 2021). Another paper entitled “Simple methods to test the accuracy of MRgFUS robotic systems” was published in the *International Journal of Medical Robotics and Computer Assisted Surgery* (Accepted: May 2021).

Journal Publication NO 1

Ultrasonics 113 (2021) 106357

Contents lists available at ScienceDirect

Ultrasonics

journal homepage: www.elsevier.com/locate/ultras

Characterization of a soft tissue-mimicking agar/wood powder material for MRgFUS applications

Theocharis Drakos [a], Marinos Giannakou [a], Georgios Menikou [b], Georgios Constantinides [c], Christakis Damianou [d,*]

[a] MEDSONIC LTD, Limassol, Cyprus
[b] Medical Physics Sector, State Health Services Organization, Nicosia General Hospital, Nicosia, Cyprus
[c] Department of Mechanical Engineering and Materials Science and Engineering, Cyprus University of Technology, Limassol, Cyprus
[d] Department of Electrical Engineering, Computer Engineering and Informatics, Cyprus University of Technology, Limassol, Cyprus

ARTICLE INFO

Keywords:
Tissue-mimicking materials
Agar
Ultrasound
MRgFUS

ABSTRACT

This study describes the development and characterization of an agar-based soft tissue-mimicking material (TMM) doped with wood powder destined for fabricating MRgFUS applications. The main objective of the following work was to investigate the suitability of wood powder as an inexpensive alternative in replacing other added materials that have been suggested in previous studies for controlling the ultrasonic properties of TMMs. The characterization procedure involved a series of experiments designed to estimate the acoustic (attenuation coefficient, absorption coefficient, propagation speed, and impedance), thermal (conductivity, diffusivity, specific heat capacity), and MR properties (T_1 and T_2 relaxation times) of the wood-powder doped material. The developed TMM (2% w/v agar and 4% w/v wood powder) as expected demonstrated compatibility with MRI scanner following images artifacts evaluation. The acoustic attenuation coefficient of the proposed material was measured over the frequency range of 1.1–3 MHz and found to be nearly proportional to frequency. The measured attenuation coefficient was 0.48 dB/cm at 1 MHz which was well within the range of soft tissue. Temperatures over 37 °C proved to increase marginally the attenuation coefficient. Following the transient thermoelectric method, the acoustic absorption coefficient was estimated at 0.34 dB/cm-MHz. The estimated propagation speed (1487 m/s) was within the range of soft tissue at room temperature, while it significantly increased with higher temperature. The material possessed an acoustic impedance of 1.58 MRayl which was found to be comparable to the corresponding value of muscle tissue. The thermal conductivity of the material was estimated at 0.51 W/m K. The measured relaxation times T_1 (844 ms) and T_2 (66 ms) were within the range of values found in the literature for soft tissue. The phantom was tested for its suitability for evaluating MRgFUS thermal protocols. High acoustic energy was applied, and temperature change was recorded using thermocouples and MR thermometry. MR thermal maps were acquired using single-shot Echo Planar Imaging (EPI) gradient echo sequence. The TMM matched adequately the acoustic and thermal properties of human tissues and through a series of experiments, it was proven that wood concentration enhances acoustic absorption. Experiments using MR thermometry demonstrated the usefulness of this phantom to evaluate ultrasonic thermal protocols by monitoring peak temperatures in real-time. Thermal lesions formed above a thermal dose were observed in high-resolution MR images and visually in dissections of the proposed TMM.

1. Introduction

The need for developing novel diagnostic and therapeutic applications that demonstrate improved safety, efficiency, and specificity towards the battle against serious diseases is a matter of ongoing research. Although phantoms were initially developed, characterized, and calibrated for ultrasound (US) imaging applications in the 60 s, there is still an undeniable need for developing new phantoms to fill the gap of emerging medical applications. Throughout the years, several efforts have been made by researchers towards developing anthropomorphic phantoms for medical teaching and imaging applications. In the field of High-Intensity Focused Ultrasound (HIFU), a reusable TMM that

* Corresponding author.
E-mail addresses: gmenicou@mphs.moh.gov.cy (G. Menikou), g.constantinides@cut.ac.cy (G. Constantinides), christakis.damianou@cut.ac.cy (C. Damianou).

https://doi.org/10.1016/j.ultras.2021.106357
Received 26 May 2020; Received in revised form 29 December 2020; Accepted 6 January 2021
Available online 30 January 2021

possesses thermal, mechanical, MR, and acoustic properties close to that of soft tissue is of outermost importance.

There are limited commercial phantom options available such as those by ONDA (Onda Corporation, 1290 Hammerwood Ave, Sunnyvale, CA 94089, USA) which are useful for Magnetic Resonance-guided Focused Ultrasound (MRgFUS) systems. Ideally, TMMs should have approximately the same ranges of the speed of sound, attenuation, absorption, and scattering coefficients as soft tissue. These features should be controllable using appropriate additives and the variability of their properties should be small at standard operating conditions.

Different types of phantoms can be found in the literature for reproducing soft tissue using different TMMs. These types of phantoms can be uniform single-component phantoms and more complex ones that mimic the specific anatomy of human tissue [1]. TMMs for MRgFUS applications present different advantages and disadvantages concerning preparation complexity, cost, and acoustic properties.

Gelatin has been widely used as a material to mimic soft tissue for US and MR imaging [2]. Gelatin-based TMMs demonstrate thermal repeatability for low acoustic power, exhibit a nearly linear stress-strain curve, provide a wide range of stiffness that is easily controllable whereas its preparation procedure is simple [3]. However, gelatin-based materials continue to stiffen over time and have a low melting point (45 °C) making them unsuitable for applications such as HIFU [4]. The attenuation coefficient of gelatin-based TMMs can be controlled by varying the amount of gelatin [5]. Amongst their reported disadvantages is that they are not always homogeneous and are susceptible to microbial and bacterial invasion [6].

Another TMM that is useful for testing MRgFUS applications is polyacrylamide. Polyacrylamide gels can be transparent thus allowing visual observation of the coagulated zone by adding some heat-sensitive contents such as bovine serum albumin (BSA) and egg-white [7–9]. The acoustic attenuation can be adjusted by using materials such as evaporated milk, intralipid, and corn syrup [10]. However, the addition of high concentration of these materials might affect the transparency of polyacrylamide gels. The coagulation temperature of these gels is comparatively higher than that of biological tissues leading to an inaccurate simulation of tissue coagulation during thermal therapies [7]. A serious safety disadvantage of polyacrylamide-based gels is that their main constituent acrylamide monomer is a known neurotoxin which is classified as a carcinogen [9]. This type of gels also exhibits a limited shelf life from several hours when exposed to air to a few weeks when stored in an airtight container [11]. ONDA Corporation produces commercially available polyacrylamide-based phantoms for characterizing ultrasonic protocols. The position and lesion shape evolution in the gel can be observed since it permanently turns opaque when temperature surpasses a threshold of 70 °C [12]. Therefore, these phantoms are used to perform quality assurance tests on HIFU systems and treatment protocol evaluation. Although polyacrylamide TMMs have a low attenuation coefficient, the addition of glass beads can be used to increase their attenuation coefficient and match the corresponding value of the human liver [8].

N-isopropylacrylamide (NIPAM) gels exhibit higher transparency at room temperature than egg white doped TMMs [13]. A large opacity change can be achieved even with a small temperature change. The formation of thermal lesion is a reversible effect making this type of TMM reusable and ideal to model the therapeutic effects of HIFU. Sun et al. [13] investigated only the ability of the NIPAM-based gel to form thermal lesions and it has not been characterized for its acoustical, thermal, and MR properties.

In a recent study by Eranki et al. [14], an MR-imageable and HIFU-compatible tissue-mimicking thermochromic acrylamide-based material was presented. Silicon dioxide and BSA were added to enhance ultrasound attenuation and MRI signal changes since the coagulation of BSA causes changes in T_2 relaxation time. A thermochromic ink that changes color based on temperature change after HIFU exposure was also used. The TMM can permanently change color upon heating, thus providing information on ablation volume geometry, spatial targeting accuracy, and quantification of heating. The thermochromic acrylamide-based material is potentially useful for testing MRgFUS applications but its use is hindered by the rather complex and long fabrication procedure.

Poly (vinyl alcohol) (PVA) materials have been also used in MR applications [15] and to mimic breast tissue [16]. PVA is a widely used non-toxic industrial material. The main disadvantage of these materials (in form of pure gel for 1–2 freeze–thaw cycles) is their low acoustic attenuation coefficient which is far lower than the majority of human soft tissue's attenuation coefficient [15]. However, with the addition of additives (enamel paint) and the increase in the number of freeze–thaw cycles, the attenuation can be further increased. The attenuation of a pure PVA-gel with 1 freeze–thaw cycle is stated to be very low at 0.075 dB/cm-MHz and increases to 0.28 dB/cm-MHz when the gel is produced with 4 freeze–thaw cycles [15]. The procedure to manufacture a pure PVA-based TMM is very long and can last for many days depending on the number of freeze–thaw cycles.

Tofu is another material used to develop TMM phantoms. Although Tofu is cheap and it is readily available, it exhibits a lower nonlinearity parameter compared to soft tissue [17]. The acoustic properties of Tofu are not adjustable and vary according to the brand of raw material and extraction method. It has also been reported that Tofu-based TMMs are susceptible to microbial invasion and their shelf life is limited [17]. However, Tofu's absorption and speed characterization replicate adequately the corresponding of human soft tissue.

Agar is also used for the development of phantoms destined for ultrasound imaging and HIFU applications. Agar-based TMMs need to be refrigerated for extending their shelf life and reusability [18]. Agar possesses a higher melting point and superior fracture toughness compared to gelatin gels of similar density and during ultrasound imaging, its echogenicity is similar to human soft tissue [18]. Amongst the advantages of agar against other TMMs is their faster production procedure, and low acoustic scattering coefficient [18,19]. A main limitation of agar is that it tends to be more expensive than gelatin. Agar-based TMMs doped with homogenized whole milk and bovine milk have an attenuation coefficient in the range of 0.35–0.4 dB/cm-MHz while the addition of evaporated milk increases the value to 0.8 dB/cm-MHz [19]. The speed of sound of pure agar-based gel (with 2% w/v agar) was estimated at 1490 m/s. According to this study [19], more agar percentage results in a higher speed of sound (1512 m/s for 7.5% w/v agar). An agar-based breast-mimicking material with the addition of silicon dioxide and evaporated milk was proposed for evaluation of focused US systems on patients with breast cancer [20]. Lately, Menikou et al. [21] introduced an agar-based head phantom with an attenuation coefficient close to the corresponding human attenuation value for HIFU applications.

There is limited literature on the effects of thermal, acoustic, mechanical, and MR properties of wood powder. The propagation speed and attenuation coefficient of various kinds of wood have been previously measured [22–24]. It has been shown that absorption linearly increases with frequency up to 4 MHz while the propagation speed is dependent on the moisture content of wood [25]. The density of wood powder and water absorption of wood powder composited with bagasse was calculated and compared to other materials [26]. The density of wood powder was found to be 0.42 gr/cm^3 and the water absorption in composite wood powder and bagasse was found to be 13.5% [26]. In a study by Ababneh [27], it was found that wood blocks (Rhizophora spp) are low-cost, stable over time and possible human breast tissue replicating material for MRI purposes. T_1 and T_2 relaxation times of wood were found to match closely the ones of breast tissue.

The purpose of this study aims to describe the development of a novel agar-based TMM doped with wood powder and test its suitability as such by characterizing its acoustic, thermal, and MR properties. The idea of using wood powder is to increase the absorption coefficient in a controllable manner with thermal properties similar to soft tissue. The associated T_1 and T_2 relaxation times control the image contrast of the

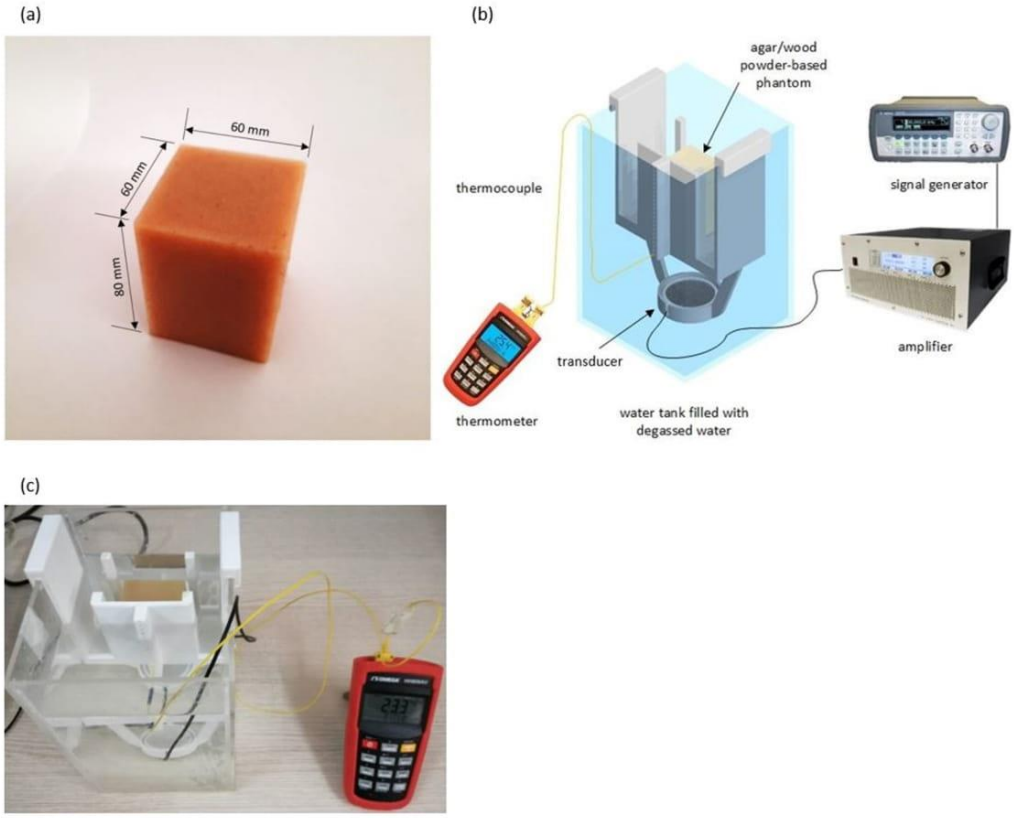

Fig. 1. (a) Photo of the developed agar/wood powder-based TMM, (b) schematic diagram of the experimental setup to measure the absorption coefficient of the TMM, and (c) photo of the experimental setup.

material in conventional MRI sequences. Wood powder is a very attractive additive since it is an abundant industrial furniture waste and most likely free of cost unlike other materials (silicon dioxide, BSA) which are more expensive and require difficult and long production procedures by the manufacturers.

Following test and trial, an appropriate agar concentration was selected to provide moderate strength to the final material in order to resist HIFU forces without cracking. The percentage of agar (2% w/v) was sufficient to create a compact material. It was chosen to avoid adding preservatives to the recipe to prolong the material's shelf-life since many of them are known of being toxic [28].

2. Materials and methods

2.1. Soft tissue-mimicking material preparation

The agar was in granular form with a particle size of 1400 μm stated in the manufacturer's datasheet (Merck KGaA, EMD Millipore Corporation, Darmstadt, Germany). The agar was initially ground to powder using a blender machine to aid mixing in water and result in a homogeneous gel. Ultrapure degassed/deionized water was slowly heated and continuously stirred using a magnetic stirrer (SBS, A160, Steinberg Systems, Germany) over a period of 10 min. The temperature increase was monitored using an electronic thermometer (Omega Thermometer, HH806AU, Omega Engineering, Norwalk, Connecticut, USA). Once the degassed/deionized water reached 50 °C, 2% w/v agar was slowly added to mitigate aggregation of the agar in the degassed/deionized water. A certain amount of agar was added to the mixture to achieve a 2% w/v agar concentration. The wood powder (Swedish pine) was further ground with an average particle size of approximately 150 μm. The average particle size was estimated by quantitative analyzing images collected on a Scanning Electron Microscope (SEM) image (FEI, Quanta 200, Hillsboro, Oregon, United States), using the open-source software Gwyddion [29]. Prior to the SEM investigation, all samples were sputter-coated with a thin (<10 nm) silver layer to reduce electron charging effects. Images were collected at 5 kV to 20 kV accelerating voltages in various magnifications.

When agar was completely dissolved in water, a proportionate amount of wood powder (Swedish pine) was added to the mixture so that the w/v concentration of wood powder to be 4%. The mixture was stirred until the temperature reached 85 °C. The mixture began to solidify once the temperature dropped (at around 50 °C). The amount of evaporated water added to equate the initial mixture volume prior to boiling initial volume. The solution was stirred with a low-speed setting to avoid trapping air bubbles in the mixture that would cause serious reflections of the HIFU beam. The whole preparation and development procedure was simple, fast, and it lasted around 20–25 min for a volume of 300 cm^3. The solution was then poured into a mold ($6 \times 6 \times 8$ cm^3) and was let to jellify overnight at room temperature. The prepared phantom was tested in ablation experiments within 24 h after its fabrication.

The wood powder obtained from a carpentry company contained large pieces of particles that may have affected the acoustic properties of the developed TMM and induced susceptibility artifacts in MRI images. It was expected that since wood powder is poor in hydrogen it would appear hypointense in MRI images. The agar/wood powder TMM presented a moderate hardness along with a light brown color as shown in Fig. 1a.

2.2. Estimation of the attenuation coefficient

Attenuation measurements were conducted using the through-

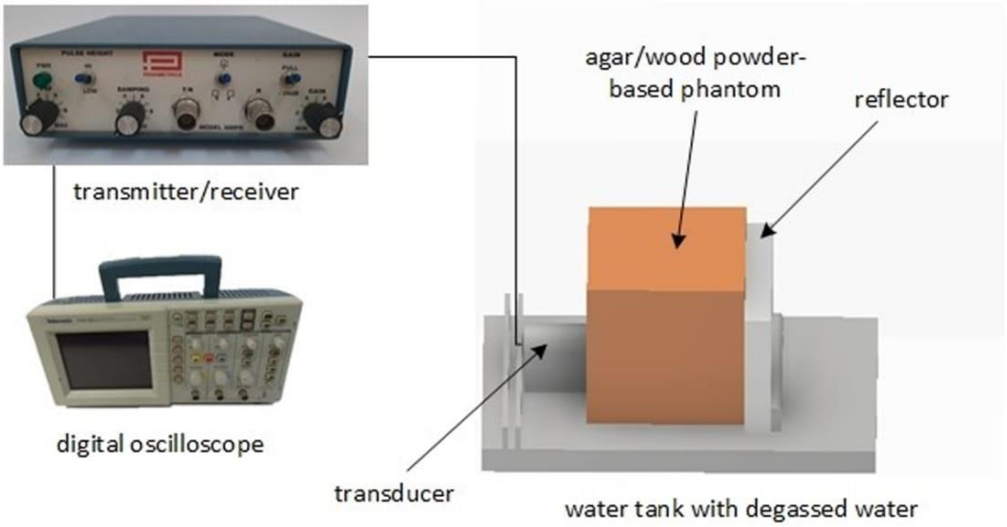

Fig. 2. Schematic diagram of the experimental setup to measure the ultrasonic propagation speed of the TMM.

transmission technique previously described by Madsen et al. [30]. The through-transmission technique involved two planar transducers; one for transmitting a pulsed US signal and one for receiving it. A special acrylonitrile butadiene styrene (ABS) plastic holder that hosts the two transducers, was designed (Inventor Professional 2018, Autodesk, California, USA) and printed using a 3D printer (F270, Stratasys Ltd., Minessota, USA). The ABS holder retained the planar transducers in cylindrical cavities with their active elements facing each other and the sample at fixed positions. Three pairs of planar immersion transducers (12 mm diameter, nominal frequency at 1.1, 2 and 3 MHz, Piezo-technologies, Indianapolis, IN, USA) were used. All pairs of transducers have an approximate ± 0.5 MHz bandwidth, thus covering a 1–3 MHz span of frequencies. A pulsed signal was transmitted using a pulser/receiver system (Panametrics 500PR, Olympus Corp, Tokyo, Japan), propagated through a 26 mm sample and received by the receiving transducer which was located 65 mm from the transmitter. The attenuated resulting signal was recorded by the receiver and displayed on a digital oscilloscope (TDS 2012, Tektronix, Inc., Karl Braun Drive, United States). The sample was positioned in the near field of the emitting transducer. The attenuation coefficient was measured over a frequency range of 1.1–3 MHz at room temperature (25 °C) for five batches of gels. The following equation was used to calculate the attenuation coefficient for each frequency using the through-transmission method and it was modified into Eq. (1) in units of dB/cm [31].

$$\alpha(f) = \left(\frac{20*\log_{10}\left(\frac{A_s(f)}{A_r(f)}\right)}{\Delta_\chi} \right) + \alpha_w \quad (1)$$

where A_s is the reference peak-to-peak voltage without the material, A_r is the resulting peak-to-peak voltage at the receiver side with the addition of the material between the two planar transducers, α_w is the attenuation of water, Δ_χ is the sample's thickness in cm, and f is the transmitting frequency. The attenuation coefficient can be frequency-dependent according to $\alpha = \alpha_o * f^n$, where α is the attenuation coefficient parameter, α_o is the attenuation coefficient at 1 MHz, and n is the power to which frequency is raised in MHz. The impact of temperature on the attenuation coefficient was examined in a temperature range from 25 to 55 °C for the tested frequency of 1.1 MHz.

2.3. Estimation of the absorption coefficient

A method to estimate fast and accurately the absorption coefficient of the material using a novel experimental setup was previously described by our group [32]. According to this methodology, the material was exposed to a focused US beam and the absorption coefficient was determined by measuring the rate of temperature rise using a thermocouple (5SC-TT-K-30–36, type K insulated beaded wire, 100 μm thick, Omega Engineering, Norwalk, Connecticut, USA). For the absorption coefficient measurement, a signal generator (HP 33120A, Agilent technologies, Englewood, CO, USA), an RF amplifier (AG1012, T & C Power Conversion, Inc., Humboldt St., Rochester, NY) and a spherically focused transducer (Sonic Concepts, Inc., Seattle, USA) operating at 0.4 MHz (focal length of 70 mm and diameter of 40 mm) were utilized in the experimental setup as described by Drakos et al. [32]. A temperature reader (HH806AU, Omega Engineering) was used to record the temperature over time in the TMM. The thermocouple was placed at the focal position which was located 3.5 cm deep from the bottom face of the TMM (the transducer was 3.5 cm below the front surface of the TMM facing upwards). Fig. 1 illustrates the schematic diagram (b) and a photo (c) of the experimental setup to estimate the absorption coefficient.

2.4. Estimation of acoustic propagation speed in soft tissue-mimicking material using the pulse-echo technique

A pulse-echo measurement immersion technique was employed for estimating the ultrasonic propagation speed of the TMM. The propagation speed was measured in a temperature range from 25 to 55 °C for the tested frequency of 1.1 MHz. The samples were immersed in a tank filled with degassed/deionized water. This technique involved a single unfocused transducer (the same transmitting transducer that was used for the attenuation measurements) to transmit and receive the reflected ultrasonic signal. The transducer transmitted pulses driven by a Panametrics pulser/receiver system (Panametrics 500PR, Olympus Corp). A digital oscilloscope (TDS 2012, Tektronix, Inc.) was connected to the pulser/receiver for observing the received signal. A thick sample of 5.8 cm was chosen to increase echoes time difference and derive a more accurate estimation of the ultrasonic propagation speed in the sample. As shown in Fig. 2, the signal was transmitted directly in the sample and reflected using a metal reflector. The propagation speed in the sample was estimated by measuring the time difference (Δ_t) between the echoes

returning from the interfaces of the sample. Eq. (2) was used to estimate the ultrasonic propagation speed (C_s) of the TMM, where d represents the thickness of the sample.

$$C_s = \frac{2d}{\Delta_t} \quad (2)$$

2.5. Mass density measurement using water volume displacement method

Mass density was estimated by measuring the mass and volume of the samples. A 50 mL TMM was prepared and sliced in equal volumes to be placed inside a volumetric tube. Each piece was first weighed with a high precision (±0.01 g) digital scale (1479 V, Tanita Corporation of America, Inc, USA) and then its volume was extracted by measuring water displacement in a volumetric tube. The accuracy of the volumetric tube (±0.1 mL) played an important role in the error of the measurements, therefore large specimens were tested to minimize the fractional error in volume measurements. Five specimens from the same batch were obtained and the average mass density in g/cm^3 was calculated.

2.6. Estimation of soft tissue-mimicking material thermal properties

The thermal properties of the aforementioned TMM were measured using the instrument Isomet (model 2104, Applied Precision, Ltd., Bratislava, Slovakia). The instrument was used according to the manufacturer's recommendation for estimating thermal conductivity (W/m K), thermal diffusivity (mm^2/s), and specific heat capacity (kJ/kg K). The transient method was used to perform the thermal conductivity measurements, which were carried out automatically by a needle sensor. The selected sensor was able to accurately measure in the range of 0.2–1 W/m K. According to the manufacturer, the accuracy of the device for thermal conductivity measurements was 5% of reading +0.001 W/m K. Thermal diffusivity is derived by dividing conductivity with density whereas specific heat capacity describes how quickly a material reacts to a change in temperature. A spherical volume of the material around the needle probe with a minimum diameter of 5 cm was needed for accurate measurement. Due to this limitation of the system, a specimen of appropriate dimensions (5 cm height, 7 cm wide, and 15 cm long) was prepared. The needle probe was inserted in the TMM and the 3 thermal properties (thermal conductivity, thermal diffusivity, and specific heat capacity) were calculated simultaneously by the device. The procedure was repeated five times and the mean and standard deviation values of each thermal property were deduced.

2.7. Experimental setup and HIFU sonication parameters

The absorption experimental setup described previously was used to apply high-power sonication in the phantom. The scope of the high-power sonication was to test the ability of the phantom to reach high temperatures and create lesions. The phantom was fitted tightly into the holder and a transducer (frequency 2.6 MHz, diameter: 38 mm, focal length: 61 mm, MEDSONIC LTD, Limassol, Cyprus) was positioned below the phantom facing upwards for a bottom to top sonication inside an acrylic water tank filled with degassed/deionized water. The experimental HIFU system included a signal generator (HP 33120A, Agilent Technologies), a radio-frequency power amplifier (AG1012, T & C Power Conversion, Inc.), and the spherically-focused transducer.

Prior to sonication, the phantom was allowed to reach thermal equilibrium with the degassed/deionized water to minimize conduction effects. During the high-power sonication, a continuous-wave mode of acoustic power of 44 W was applied. The duration of the sonication was 30 s. The transducer position was adjusted in order to focus at 2 cm deep inside the phantom. Post-HIFU, the phantom was dissected to look for a thermal lesion. Multiple lesions were also created in an identical phantom for repeatability purposes.

2.8. Temperature measurement using a thermocouple

During a high-power sonication, the temperature change at the focal point of the phantom was recorded. The temperature reader (HH806AU, Omega Engineering) was used to record the temperature change in the phantom. The thermocouple (5SC-TT-K-30–36, type K insulated beaded wire, 100 μm thick, Omega Engineering) was inserted in the sample at the focus which was 2 cm deep. The thermocouple tip was rigid enough and it was inserted from one end of the phantom, all the way to the target with the phantom immersed in degassed/deionized water. The thermocouple tip was selected to be sufficiently thin to reduce possible artifacts. MRI artifacts were also avoided due to the size of the thermocouple. The thermocouple did not carry any electricity and therefore was considered as a passive object in the MR imaging volume. Although the focal length was known, precise localization of the focal point was achieved by changing the position of the thermocouple at low power until the highest temperature change was achieved.

2.9. Ultrasound and X-ray imaging

A diagnostic US imaging system (UMT-150, Shenzhen Mindray Bio-Medical Electronics Co., Ltd., Shenzhen, P.R. China) was used to image the TMM in order to check its echogenicity and homogeneity. A homogeneous piece of swine meat was US scanned with the same ultrasonic parameters to be compared with the US image of the TMM. An X-ray image was also acquired using a portable X-ray system (IMS001, Shenzhen Browiner Tech Co., Ltd., Shenzhen, P.R. China). A computed radiography (CR) reader (Vita Flex, Carestream Health, Inc., 150 Verona Street, Rochester, NY, USA) was used to digitize the latent image from the CR cassette to the computer for X-ray image reconstruction. The X-ray exposure parameters were as follows: tube current = 50 mA, tube voltage = 60 kV, and an exposure time of 320 ms.

2.10. MR imaging and thermometry

High-resolution MR images of the phantom were acquired after HIFU sonication in a 1.5 T MR system (Signa Excite, General Electric, Fairfield, CT, USA) using a GPFLEX coil (USA instruments, Cleveland, OH, USA). Proton density (PD) MR images were acquired with the following parameters: repetition time (TR) = 2420 ms, echo time (TE) = 41 ms, receiver bandwidth (rBW) = 15 kHz, matrix = 256 × 256 pixels, slice thickness = 3 mm, number of excitations (NEX) = 7, and displayed field of view (DFOV) = 25 × 25 cm^2.

The temperature change in the phantom under HIFU sonication was assessed with MR thermometry. MR thermometry data was produced using single-shot EPI with the following parameters: TR = 80 ms, TE = 25.1 ms, rBW = 15 kHz, matrix = 64 × 64 pixels, slice thickness = 3 mm, NEX = 1, flip angle = 25°, and DFOV = 25 × 25 cm^2.

The phantom was sonicated with the same transducer used during the thermocouple's temperature change recordings. Temperature changes were calculated using the proton resonance frequency shift method [33]. The thermometry slice was selected in a plane parallel to the propagation direction. Coronal thermal maps were initially obtained by applying low acoustical power to observe the temperature increase in the phantom and to detect the focal spot of the transducer. When the focal spot was detected, axial thermal maps were recorded to estimate the temperature change and observe the focal beam in the axial plane (parallel to the ultrasonic beam). Following analysis, a single thermal map was produced every 1.65 s. The applied acoustical power was 44 W for a sonication time of 30 s using the 2.6 MHz spherical transducer.

2.11. T_1 and T_2 relaxometry

The TMM was scanned in the MRI using the GPFLEX coil (USA instruments) to estimate the relaxation times. The methods to estimate the T_1 and T_2 relaxation times have been previously described in detail by

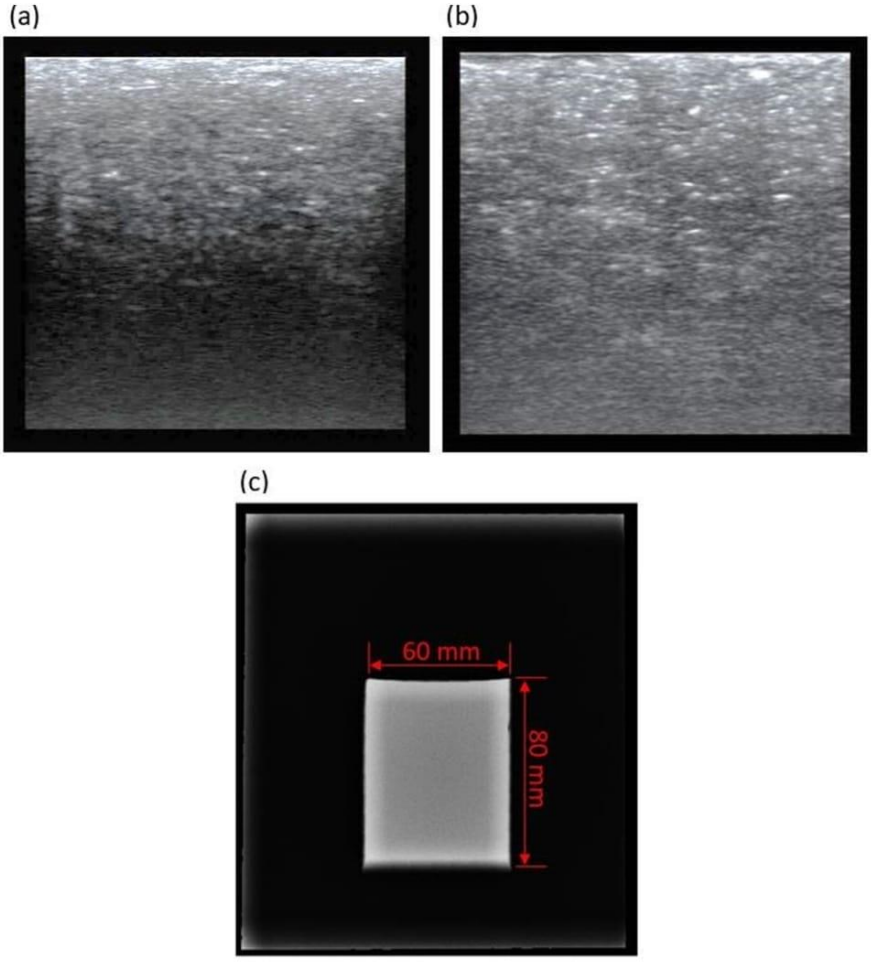

Fig. 3. (a) US image of the TMM with 2% w/v agar and 4% w/v wood powder, (b) US image of a soft tissue (swine meat), and (c) X-ray image of the TMM.

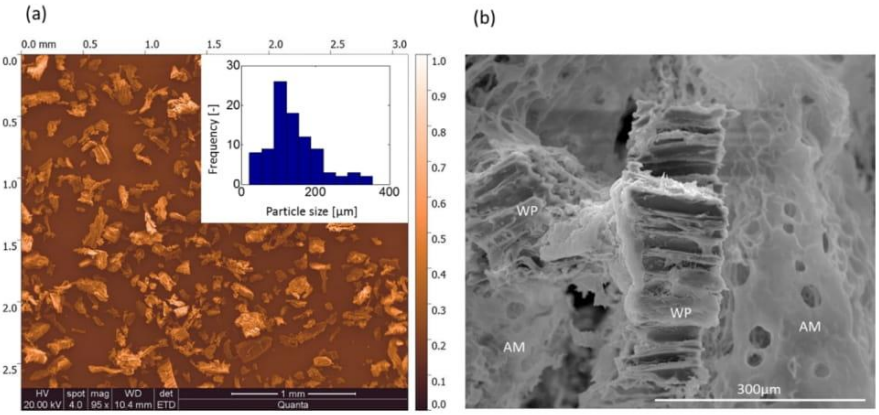

Fig. 4. SEM images of the (a) wood powder (a histogram of 92 particle length measurements is shown in inset) and, (b) agar/wood powder TMM (WP = wood powder particles, AM = agar matrix).

Menikou et al. [33]. For measuring the spin–lattice relaxation time (T_1), an Inversion Recovery Fast Spin Echo (IR-FSE) sequence with the following acquisition parameters were used: TR = 3000 ms, TE = 45 ms, slice thickness = 5 mm, NEX = 4, matrix = 256 × 256 pixels, and variable Inversion Time (TI) = 200, 400, 800, 1200, and 1600 ms.

The T_2 relaxation time was estimated by obtaining a series of Fast Spin Echo (FSE) sequences for different effective echo times (23, 34, 45, 68, and 101 ms) and by calculating the inverse exponent of the exponential fit. The other MR parameters were: TR = 2500 ms, slice thickness = 5 mm, matrix = 256 × 256 pixels, FOV = 16 cm, NEX = 1, and echo train length (ETL) = 4.

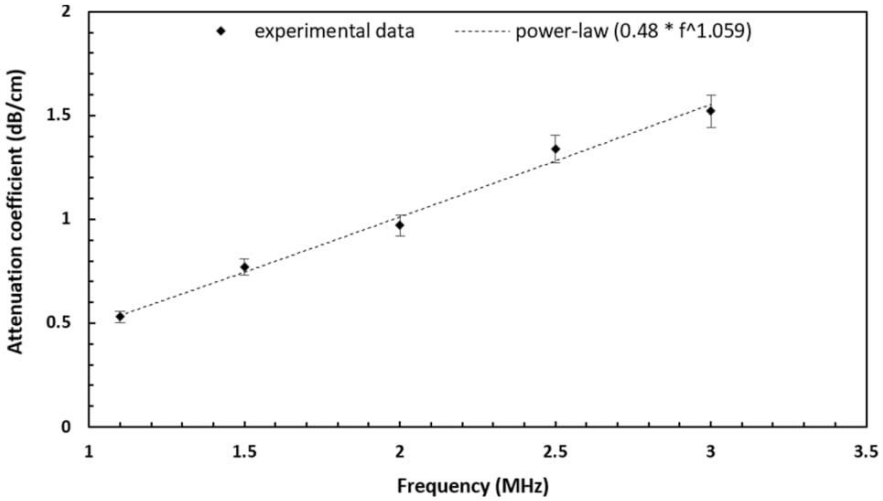

Fig. 5. Attenuation coefficient as a function of frequency for the agar/wood powder-based TMM. The mean and standard deviation are represented by the data points and the error bars respectively.

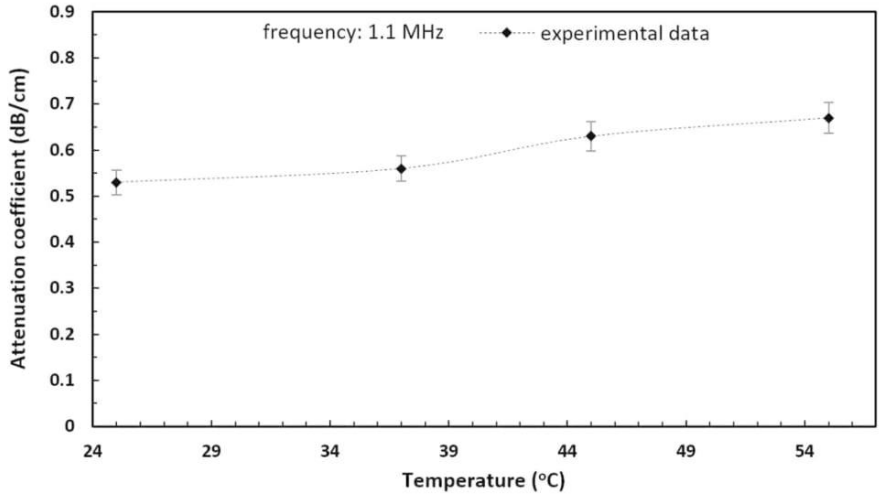

Fig. 6. Attenuation coefficient as a function of temperature for a frequency of 1.1 MHz. The mean and standard deviation are represented by the data points and the error bars respectively.

3. Results

An agar-based doped with wood powder TMM was prepared following a simple and fast procedure. The gel with 2% w/v agar and 4% w/v wood powder was scanned with a US imaging system (UMT-150, Shenzhen Mindray Bio-Medical Electronics Co., Ltd.) in order to demonstrate that wood powder contributes to US scattering. The scattering of the wood powder has been shown to contribute to the absorption and therefore to a total attenuation increase. The TMM appeared homogeneous with increased echogenicity as shown in Fig. 3a. Fig. 3b shows the US image of a homogeneous soft tissue (swine meat). The grey texture of the TMM resembled the sonographic appearance of normal soft tissue. Fig. 3c shows the X-ray image of the TMM.

SEM images of the wood powder and agar/wood powder TMM are illustrated in Fig. 4a and b, respectively. The wood powder particles appear elongated with aspect ratios in the range of 1–5. Statistics on the particle size were extracted by performing line measurements using the open-source software Gwyddion on the long direction of approximately 90 particles (Fig. 4a). A range of 20–350 μm was recorded with an average particle size in the ~140 μm range and a standard deviation of ~70 μm.

A least mean square fitting was fitted on the attenuation coefficient measurements of various frequencies between 1.1 and 3 MHz. The measured attenuation coefficient (α_o) was 0.48 ± 0.044 dB/cm at 1 MHz which was well within the range of equivalent values of soft tissue [34,35]. A power-law fit was determined on the data and the parameter n was found to be 1.059, which for the range of frequencies used in HIFU it is safe to assume that the attenuation coefficient of the TMM depends linearly on frequency. Fig. 5 shows the attenuation coefficient as a function of frequency. It was thought that the size of the wood powder particles (<350 μm) played a significant role in the value of the scattering coefficient. Wood powder particles with dimensions of the order of one wavelength of the sound wave or larger (~0.6 mm) are expected to diffract (beam spreading) the acoustic wave rather than scatter the wave in all directions. The attenuation coefficient for a frequency of 1.1 MHz at room temperature was found to be 0.53 dB/cm and the value remained almost unaffected at 37 °C. At higher temperatures, the attenuation coefficient slightly increased by reaching a value of 0.67 dB/cm at 55 °C. The effect of temperature on the attenuation coefficient is shown in Fig. 6.

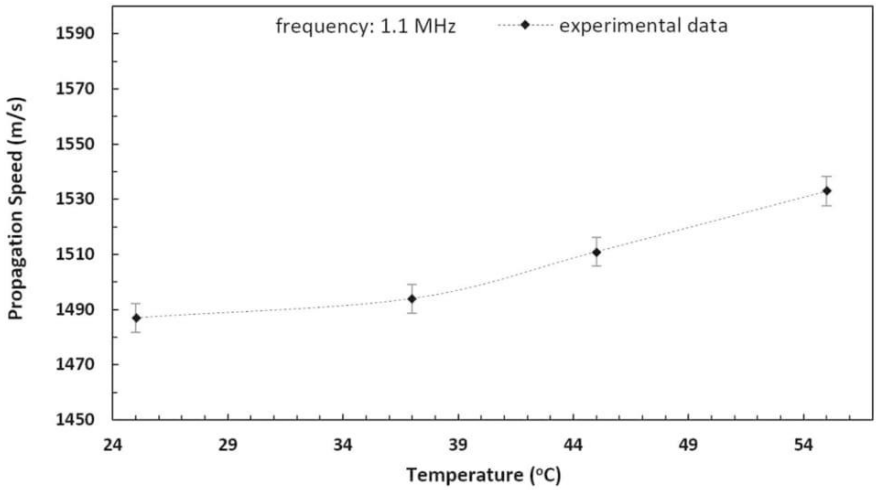

Fig. 7. Propagation speed as a function of temperature for a frequency of 1.1 MHz. The mean and standard deviation are represented by the data points and the error bars respectively.

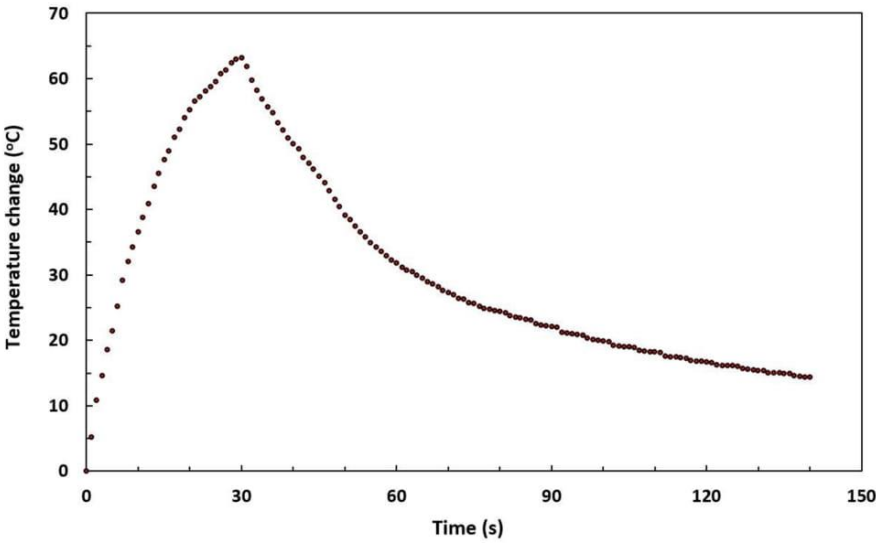

Fig. 8. Temperature change versus time that was recorded using the thermocouple by applying an acoustic power of 44 W for 30 s at a focal depth of 2 cm with the 2.6 MHz spherically-focused transducer.

Acoustic propagation speed and mass density were also assessed. The propagation speed was 1487 ± 5 m/s at room temperature which is a value between the speed of sound of intra-vitam fat (~1480 m/s) [34] and soft tissue (~1540 m/s) [35]. The propagation speed increased from 1487 m/s to 1533 m/s in a temperature range between 25 and 55 °C as shown in Fig. 7. Density was calculated to be 1060 ± 10 kg/m^3 using the water volume displacement method. Therefore, the acoustic impedance of the TMM was 1.58 ± 0.03 MRayl. This result indicated an acoustic impedance close to that of muscle (1.62 MRayl) [34]. Water has an acoustic impedance of 1.54 MRayl, therefore the reflected intensity in the water/TMM interface was 0.016%.

The absorption coefficient was estimated by applying an ultrasonic protocol that produces a low-temperature change between 2 and 3 °C, which corresponded to an acoustic power of 1 W. During the sonication, the temperature increased linearly with time as expected after eliminating conduction effects. The temperature maintained its linearity (with R-squared of 0.9262) for a long sonication (30 s), which is representative of low conductivity. The maximum temperature recorded was 2.7 °C, and the rate of temperature increase was 0.045 °C/s. Based on the temperature–time gradient, the absorption coefficient was 0.34 ± 0.02 dB/cm-MHz. By subtracting the estimated absorption coefficient from the attenuation coefficient, the remaining value coefficient which is attributed to non-thermal losses is found to be 0.14 dB/cm-MHz (mostly scattering). The reflection coefficient was 0.016% based on the acoustic impedance measurement.

Thermal properties (thermal conductivity, thermal diffusivity, and specific heat capacity) were assessed by inserting a needle probe in the TMM and allow the appropriate area around the needle probe for accurate measurement. The thermal conductivity, thermal diffusivity, and specific heat capacity were estimated at 0.51 ± 0.005 W/m K, 0.29 ± 0.0015 mm^2/s, and 1.76 ± 0.001 kJ/(kg K) respectively.

Temperature change measurements were performed in the phantom using thermocouples. A temperature rise of 63 °C was achieved with a HIFU duration of 30 s and 44 W as shown in Fig. 8. After the HIFU exposure, the sonicated area showed some deterioration indicating the extent of the sonicated region. Maximum HIFU temperature changes are far less than the minimum ignition temperature of wood and therefore wood powder is considered a safe material to be used in MRgFUS

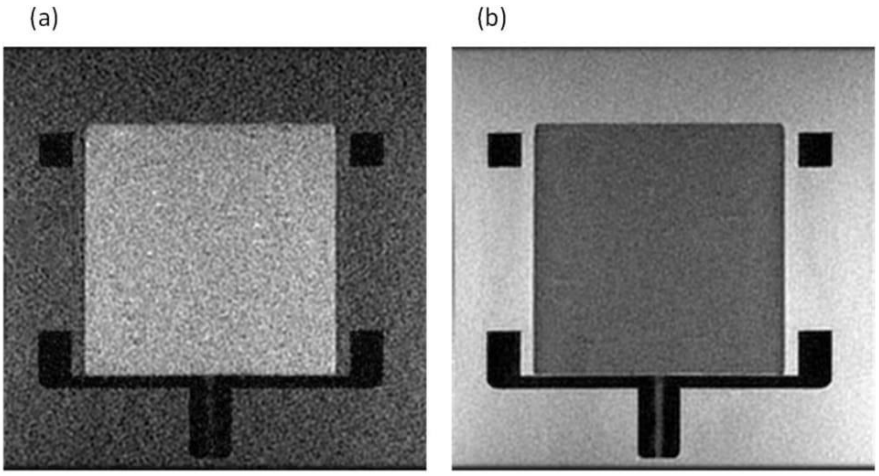

Fig. 9. (a) IR-FSE image of the TMM with TR: 3000 ms, TI: 1200 ms, and (b) T_2-weighted FSE image with TR: 2500 ms, TE: 68 ms. IR-FSE and T_2-weighted FSE images were acquired with various TI and TE times in order to estimate the T_1 and T_2 relaxation times respectively.

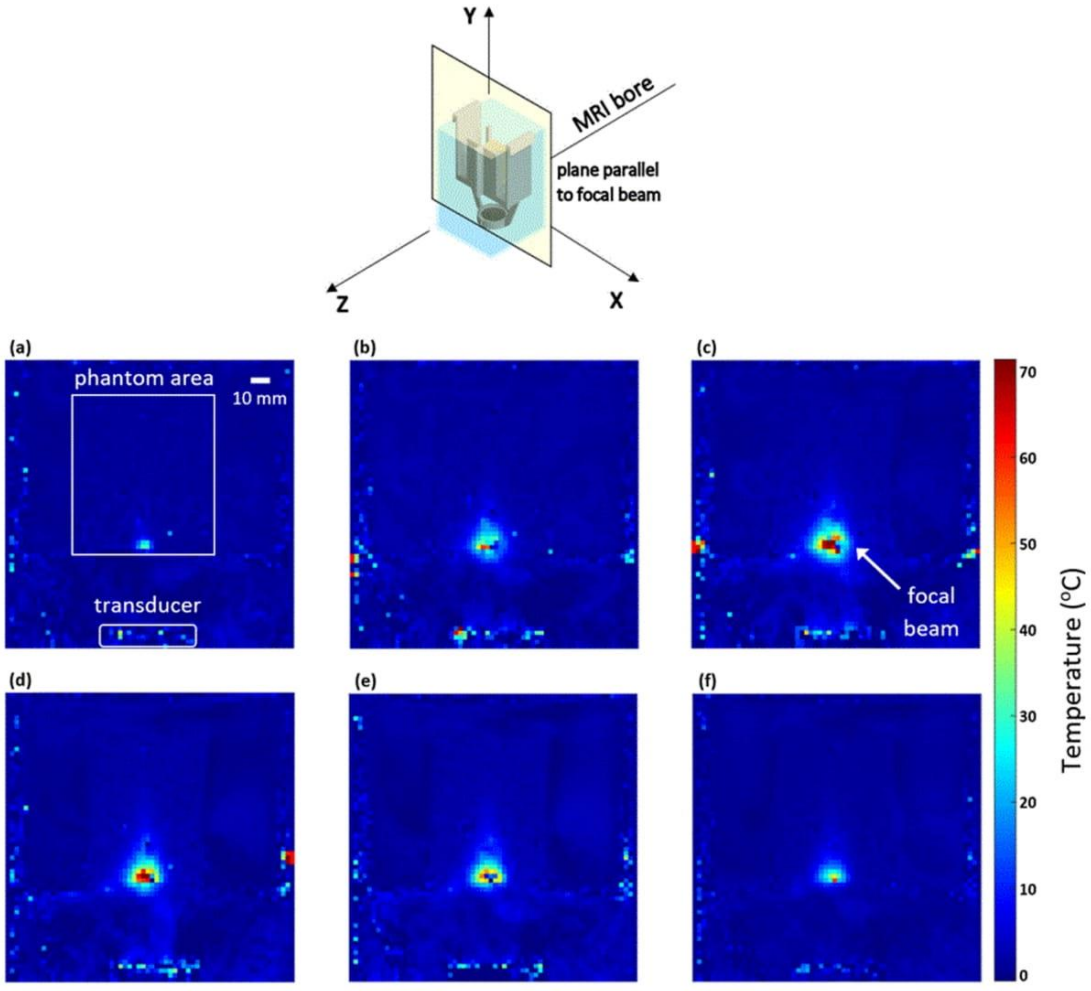

Fig. 10. MR thermal maps obtained in a plane parallel to the beam at a focal depth of 2 cm for sonication time of (a) 5 s, (b) 15 s, (c) 25 s, and (d) 30 s and for a cooling time of (e) 10 s, and (f) 18 s, respectively. The plane of the MR thermometry maps taken in relation to the direction inside the MRI is indicated.

applications.

The TMM was MR imaged using IR-T_1 FSE and T_2-weighted FSE sequences (Fig. 9a and b) in order to estimate the T_1 and T_2 relaxation parameters respectively. There were no severe artifacts in the vicinity of the TMM as expected. The best quality images, in terms of signal-to-noise ratio were taken and provided strong evidence that the TMM

Table 1
Summary of the acoustic, MR, and thermal properties of the agar/wood powder-based TMM along with the corresponding values of soft tissues and other TMMs that were found in the literature.

Property	Value	
	Agar/wood powder-based	Soft tissues/other TMMs
Attenuation coefficient	0.48 ± 0.044 dB/cm-MHz	Fat: 0.48 dB/cm-MHz [34] Liver: 0.5 dB/cm-MHz [35] Pure agar-based phantom (2% w/v): 0.18 [34] Pure PVA-based phantoms: 0.075–0.28 dB/cm-MHz [15]
Absorption coefficient	0.34 ± 0.02 dB/cm-MHz	Agar (4%)/silica (4%)/milk (30%)-based TMM: 0.22 dB/cm-MHz [32]
Propagation speed at room temperature	1487 ± 5 m/s	Soft tissues: 1478–1595 m/s [1] Intra-vitam fat: 1480 m/s [34] Pure agar-based phantom (2% w/v): 1490 m/s [19]
Mass density	1060 ± 10 kg/m^3	Brain, liver, breast: 1040–1060 kg/m^3 [39] Muscle: 1090 kg/m^3 [39] Agar-based phantoms: 1030 kg/m^3 [19]
Acoustic impedance	1.58 ± 0.03 kg/m^2 s	Muscle: 1.62 MRayl [34] Agar- and polyacrylamide-based phantoms: 1.5–1.66 MRayl [41,43]
Thermal conductivity	0.51 ± 0.005 W/m K	Non-perfused muscle: 0.5–0.6 W/m.K [44]
Thermal diffusivity	0.29 ± 0.0015 mm^2/s	Agar/silica phantom: 0.12–0.16 mm^2/s [33,45] Acrylamide-based phantom: 0.13–0.14 mm^2/s [14,41]
Specific heat capacity	1.76 ± 0.001 kJ/(kg K)	Human and animal fat: 1.6–3 kJ/(kg K) [47]
T1 relaxation time at 1.5 T	844 ms	Skeletal muscle: 868 ms, heart: 866 ms, liver: 492 ms, kidney: 652 ms [48]
T2 relaxation time at 1.5 T	66 ms	Skeletal muscle: 47 ms, heart: 57 ms, liver: 43 ms, kidney: 58 ms [48]

contained only MR compatible materials.

MR thermometry was used to calculate the maximum temperature at the focus for the same sonication protocol that was used to measure the temperature change with the thermocouple (acoustic power of 44 W for 30 s). Fig. 10 shows the estimated MR thermal maps obtained in a plane parallel to the focal beam at a depth of 2 cm. The sonication was 30 s and MR images were also acquired during the deactivation of the transducer to confirm the temperature drop. EPI sequence was used to obtain 29 MR images within a total MR scanning time of 48 s (1.65 s for each image). However, only 6 out of 29 MR images are presented in the MR thermometry results (4 during sonication and 2 during the cooling-off period). The temperature change as calculated from the thermal map at sonication of 30 s reached a value of 66.4 °C.

Following image post-processing, the nulling TI was interpolated at 585 ms and the T_1 was estimated at 844 ms. The T_2 relaxation time was found to be 66 ms. The acoustic, MR, and thermal properties of the agar-based doped with wood powder material are summarized in Table 1 along with the corresponding values of soft tissues and some TMMs. A high-resolution PD MR image was obtained after the sonication (Fig. 11a) and the sonicated area appeared brighter than the non-sonicated area. The TMM was cross-sectioned after the sonication and the sonicated brighter area was visually confirmed (Fig. 11b). The created lesion as well as its dimensions (length and diameter) are indicated in Fig. 11b. The length and diameter of the lesion were 14.5 mm and 7.8 mm respectively resulting in a ratio (length to diameter) of 1.85. Six lesions of the same HIFU parameters (44 W acoustic power for 30 s) were created as shown in Fig. 11c. The mean diameter and length of the lesions were 6.8 ± 0.5 mm and 14.4 ± 1.9 mm respectively.

A focused transducer with a lower frequency (1.1 MHz, diameter: 64 mm, focal length: 63 mm, MEDSONIC LTD) was used to produce a lesion to a greater depth within the phantom. An acoustic power of 37.5 W was applied for 30 s sonication time at a focal depth of 2.5 cm. After the sonication, the phantom was cross-sectioned at 25 mm and a lesion of 18.8 mm length was observed as shown in Fig. 12.

4. Discussion

In this study, a TMM destined to be used for MRgFUS applications has been characterized for its acoustical, MR, and thermal properties. The TMM was agar-based with the addition of a single material to control both acoustic energy loss mechanisms (absorption and scattering). This easy-to-make agar-based gel with the addition of wood powder is non-toxic, simple and quick to prepare, inexpensive cost, and possesses a high melting temperature point.

The MRI compatibility of the TMM is especially valuable since HIFU treatments are lately performed under MRI guidance [36–38]. Powdered wood with low water content produces an MRI signal with an acceptable signal-to-noise ratio. Additionally, changes in magnetic susceptibility at agar gel/wood interfaces, perturb the homogeneity of the local field and may induce artifacts capable of disturbing MR thermometry results. The issues addressed can be avoided by developing in the future a TMM of even smaller wood particles. The particle size of a sample of the wood powder was evaluated using SEM and it was estimated to be 139 ± 69 μm with a particle maximum size of 354 μm and a minimum of 22 μm.

Even though Onda Corporation produces phantoms for HIFU applications, the phantoms are expensive and a complex procedure is followed for their production. In addition, these commercial phantoms lack stability when submerged in water because they exhibit reduced rigidity. These disadvantages make them less suitable for some applications. Herein, the proposed MRgFUS TMM has good rigidity, lasts around 10 days stored in the refrigerator at a constant temperature of 4 °C, where at the end of this period it begins to dry out. However, the life of the TMM can be prolonged by the addition of preservative materials (Thimerosal or Germall-plus). The production cost of the TMM was low, therefore at the end of experimental sessions it was disposed.

The measured attenuation coefficient at 1 MHz was found to be close to fat (0.48 dB/cm-MHz) [34] and liver (0.5 dB/cm-MHz) [35]. A nearly linear frequency dependency of the attenuation coefficient has been demonstrated in a frequency range used mainly in MRgFUS applications. At body temperatures, the attenuation coefficient of the material remained almost constant relative to the same parameter at room temperature. Nevertheless, at higher temperatures, this value has shown a slightly increasing trend. The agar/wood powder TMM (manufactured with only two materials) has higher attenuation than other more complicated TMMs which have been developed and characterized over time such as agar, gelatin with the inclusion of glass bead scatterers (0.35–0.46 dB/cm-MHz) [28] and pure polyacrylamide gels (0.17–0.25 dB/cm-MHz) [34].

The measured absorption coefficient of the prescribed TMM was found to be higher by 0.12 dB/cm-MHz than an optimum recipe (4% w/v agar, 30% volume per volume evaporated milk, and 4% w/v silica) that was proposed in a previous study [32]. The goal was to increase the absorption coefficient as close as possible to 0.5 dB/cm-MHz. It was previously evidenced [32] that the absorption coefficient increases with the increase of agar concentration, evaporated milk, and silicon dioxide (until 4%). In order to observe the effect of wood powder on the absorption coefficient, a comparison between a TMM with only 2% agar and one with 2% agar and 4% wood powder was performed. The addition of 4% of wood powder increases the absorption coefficient by 0.11 dB/cm-MHz.

Measurement of the acoustic speed of the soft tissue recipe was in the lower range of biological soft tissues (1478–1595 m/s) [1] and near the value of a head-mimicking phantom that was previously proposed by our group [21]. There has been an increasing trend in the propagation speed relative to the increase in temperature. At high temperatures, the propagation speed was close to the value of soft tissue. If values closer to

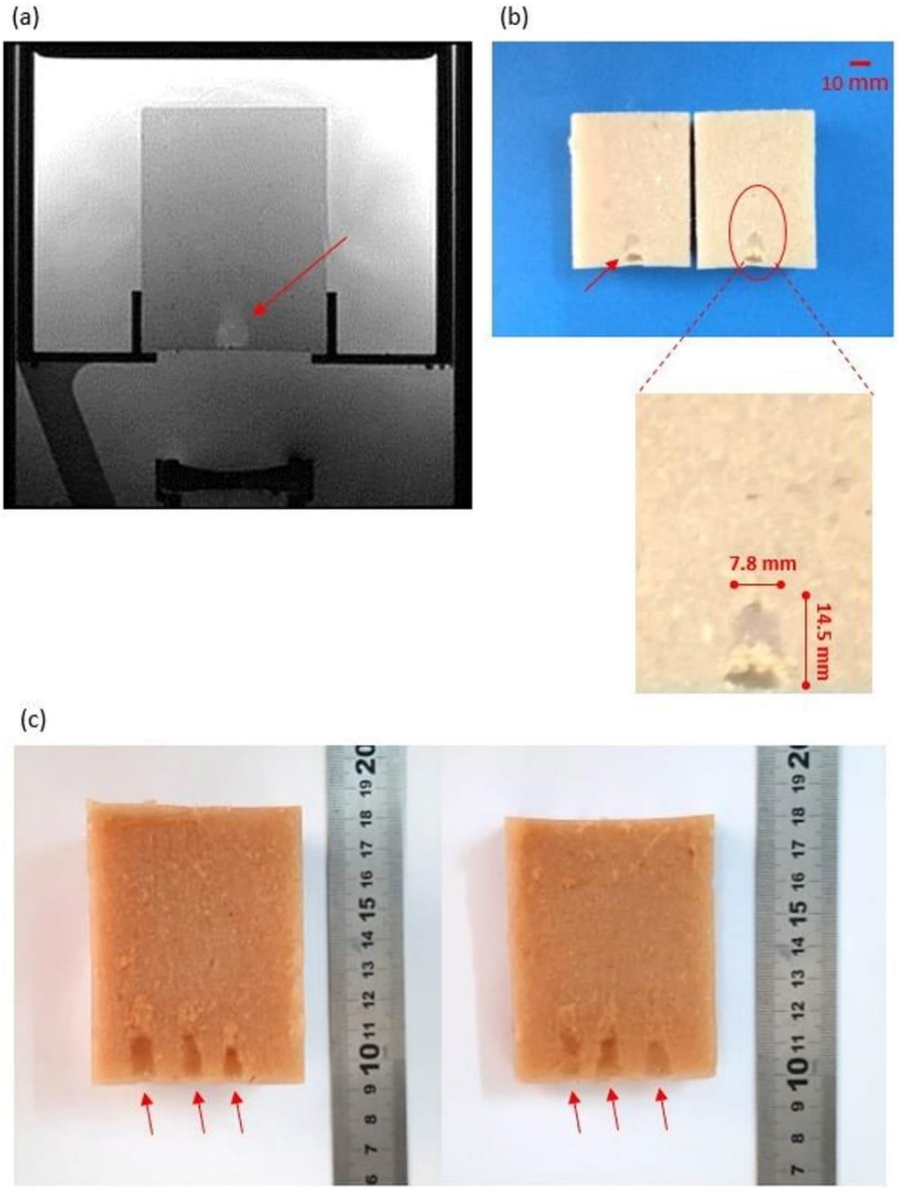

Fig. 11. (a) PD MR image of the TMM that was obtained after the sonication of acoustic power of 44 W for 30 s using the 2.6 MHz spherically focused transducer, and (b) Photo of the sonicated area. The TMM was vertically sliced in the middle of the focal spot. A zoomed image of the sonicated area shows the created lesion and its dimensions are indicated, and (c) Multiple lesions created in the TMM. The red arrows indicate the lesions.

1540 m/s are desired in low room temperatures, an appropriate concentration of an additive (glycerol or milk) can be added.

The mass density of the TMM (1060 ± 10 kg/m^3) was found to be similar to that of the brain, liver, and breast (1040–1060 kg/m^3) [39] while it approximated the mass density of muscle (1090 Kg/m^3). Gelatin and polyacrylamide gel TMMs demonstrated mass density values within the range of soft tissues [40–42] and closed values to the proposed TMM. The acoustic impedance was in the range of other agar-based and polyacrylamide-based materials (1.5–1.66 MRayl) [41,43].

The thermal conductivity (0.51 ± 0.005 W/m K) of the TMM mimics published values for non-perfused soft tissues with the value of non-perfused muscle to be in the range of 0.5–0.6 W/m K [44]. The thermal diffusivity (0.2935 ± 0.0015 mm^2/s) was more than double compared to agar/silica recipe (0.12–0.16 mm^2/s) [33,45] and acrylamide-based (0.13–0.14 mm^2/s) [14,41] which are similar to the value of water (0.143 mm^2/s) [46]. It is concluded that wood powder also contributes to the increase of the TMM's thermal diffusivity. The high thermal diffusivity shows how quickly the material transfers heat across HIFU temperatures. Specific heat capacity was in the range of the values of human and animal fat [47].

From the US images, it was shown that the addition of wood powder increased the echogenicity of the TMM, such that it closely resembled the US signal generated by real tissues. Additionally, the TMM fulfilled the requirement of being compatible with an MRI scanner. The measured relaxation times T_1 and T_2 were within the range of values found in the literature for soft tissue [48].

MRI and optical images of the TMM indicate that HIFU ablation at high power levels can lead to the formation of focal lesion. The formation of focal lesion in MRI images appears to be hyperintense. The TMM allows the lesions to be optically observed and measured. However, high power sonications cause irreversible damage to the phantom, whilst in low power settings the absence of any material deterioration

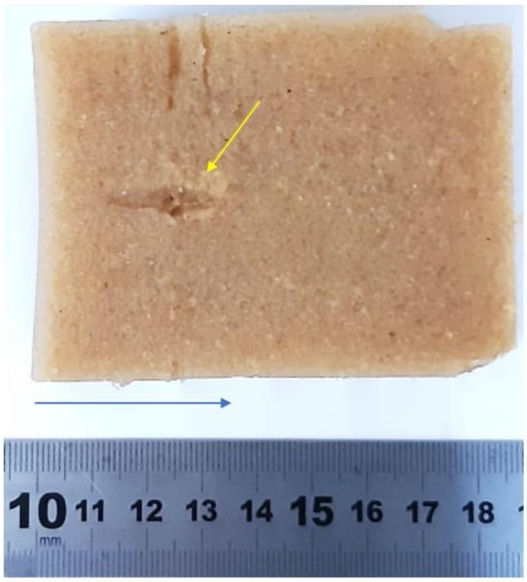

Fig. 12. A lesion was formed on a plane parallel to the ultrasound beam after HIFU exposure at acoustic power of 37.5 W for a sonication time of 30 s using a 1.1 MHz focused transducer at 2.5 cm focal depth. The yellow arrow indicates the lesion and the blue arrow indicates the beam direction.

demonstrated its suitability of being used repeatedly. Additionally, the possibility of inserting thermocouples to measure temperature rise and check transducers' performance without affecting its structural integrity was another feature of the phantom. The temperature rise measured with the thermocouple was confirmed with MR thermometry. Both thermocouple and MR thermometry yielded almost identical temperature change readings for a specific ultrasonic protocol (63 and 66.4 °C respectively). There is always a possibility that the acoustic field is distorted by the metal-base thermocouple wire, which can induce a focus shift observed as a peak temperature decrease. Positioning of the thermocouple is done manually and although all possible measures are followed to target the nominal focal region, the procedure is always prone to mispositioning errors. The main advantage of using this method is the relatively low noise of the temperature-time profile compared to MR thermometry. On the other hand, the reliability of MR thermometry results is related to the signal-to-noise ratio of the phase images which is usually limiting since the imaging coils are not optimized for the phantom's geometry. External interferences that induce inhomogeneities to the MR static field are also sources of error in MR thermometry. Mispositioning of single slice MR thermometry especially in the long axis and partial volume effect are also factors that can underestimate peak temperature.

Finally, the length to diameter ratio showed that a good-shaped lesion was created and cavitation was not affecting. The expected focal beam was at a depth of 20 mm. However, the focal beam shifted 10 mm to the front surface of the TMM. Higher penetration of the US beam can be achieved using a transducer with a lower frequency (0.5–1 MHz). This was achieved by using a transducer with lower frequency and lesion was created to a greater depth in the phantom. Multiple lesions were produced indicating repeatability of the lesions' dimensions.

5. Conclusions

A complete characterization of an agar-based TMM doped with wood powder destined for evaluation of MRgFUS protocols was presented. The characterization included measurements of the acoustical, MR, and thermal properties of the TMM. The goal of this work was to develop an agar-based TMM doped with a single material in order to achieve a higher absorption coefficient than other agar-based TMMs doped with various additives. However, the effect of the particle size of the wood powder on the acoustical, MR, and thermal properties of the TMM should be investigated further in upcoming studies. Finally, the TMM has the ability to model the formation of thermal lesions above the temperature threshold which is still unknown. In the future, when the threshold is determined it will be possible to estimate the ultrasonic energy that is needed to produce a lesion in the TMM. Future studies will entail adding materials to change the agar/wood powder TMM properties to match the properties of specific tissues of interest.

Ethical approval

This article does not contain any studies with human participants or animals performed by any of the authors.

Declaration of Competing Interest

The authors declare that they have no known competing financial interests or personal relationships that could have appeared to influence the work reported in this paper.

Acknowledgements

The study has been funded under the Restart 2016-2020 program, with the support of the Cyprus Research and Innovation foundation, and the European Structural Funds under the project SOUNDPET (INTEGRATED/0918/0008).

References

[1] M.O. Culjat, D. Goldenberg, P. Tewari, R.S. Singh, A review of tissue substitutes for ultrasound imaging, Ultrasound Med. Biol. 36 (6) (2010) 861–873, https://doi.org/10.1016/j.ultrasmedbio.2010.02.012.

[2] L. Hofstetter, L. Fausett, A. Mueller, H. Odeen, A.H. Payne, D.A. Christensen, D. L. Parker, Development and characterization of a tissue mimicling psyllium husk gelatin phantom for ultrasound and magnetic resonance imaging, Int. J. Hyperthemia 37 (1) (2020) 283–290, https://doi.org/10.1080/02656736.2020.1739345.

[3] T.J. Hall, M. Bilgen, M.F. Insana, T.A. Krouskop, Phantom materials for elastography, IEEE Trans. Ultrason., Ferroelectr., Freq. Control 44 (6) (1997) 1355–1365, https://doi.org/10.1109/58.656639.

[4] A. Dabbagh, B.J.J. Abdullah, C. Ramasindarum, N.H.A. Kasim, Tissue-mimicking gel phantoms for thermal therapy studies, Ultrason. Imaging 36 (4) (2014) 291–316, https://doi.org/10.1177/0161734614526372.

[5] J.R. Cook, R.R. Bouchard, S.Y. Emelianov, Tissue-mimicking phantoms for photoacoustic and ultrasound imaging, Biomed. Opt. Express 2 (11) (2011) 3193–3206, https://doi.org/10.1364/BOE.2.003193.

[6] E.L. Madsen, J.A. Zagzebski, R.A. Banjavie, R.E. Jutila, Tissue mimicking materials for ultrasound phantoms, Med Phys. 5 (5) (1978) 391–394, https://doi.org/10.1118/1.594483.

[7] K. Takegami, Y. Kaneko, T. Watanabe, T. Maruyama, Y. Matsumoto, H. Nagawa, Polyacrylamide gel containing egg white as new model for irradiation experiments using focused ultrasound, Ultrasound Med. Biol. 30 (10) (2004) 1419–1422, https://doi.org/10.1016/j.ultrasmedbio.2004.07.016.

[8] J.M. Choi, S.R. Guntur, K.I. Lee, D.G. Paeng, A. Coleman, A tissue mimicking polyacrylamide hydrogel phantom for visualizing thermal lesions generated by high intensity focused ultrasound, Ultrasound Med. Biol. 39 (3) (2013) 439–448, https://doi.org/10.1016/j.ultrasmedbio.2012.10.002.

[9] C. Lafon, V. Zderic, M.L. Noble, et al., Gel phantom for use in high-intensity focused ultrasound dosimetry, Ultrasound Med. Biol. 31 (10) (2005) 1383–1389, https://doi.org/10.1016/j.ultrasmedbio.2005.06.004.

[10] M. McDonald, S. Lochhead, R. Chopra, M. Bronskill, Multi-modality tissue-mimicking phantom for thermal therapy, Phys. Med. Biol. 49 (13) (2004) 2767–2778, https://doi.org/10.1088/0031-9155/49/13/001.

[11] M. Bini, A. Ignesti, L. Millanta, R. Olmi, N. Rubino, R. Vanni, The polyacrylamide as a phantom material for electromagnetic hyperthermia studies, IEEE Trans. Biomed. Eng. 31 (3) (1984) 317–322, https://doi.org/10.1109/TBME.1984.325271.

[12] ONDA Corporation, HIFU Phantom Gel, http://www.ondacorp.com/images/brochures/Onda_GelPhantom_DataSheet.pdf 2012 (accessed 20 March 2020).

[13] M.K. Sun, J. Shieh, C.W. Lo, et al., Reusable tissue-mimicking hydrogel phantoms for focused ultrasound ablation, Ultrason. Sonochem. 23 (2015) 399–405, https://doi.org/10.1016/j.ultsonch.2014.10.008.

[14] A. Eranki, A.S. Mikhail, A.H. Negussie, P.S. Katti, B.J. Wood, A. Partanen, Tissue-mimicking thermochronic phantom for characterization of HIFU devices and

applications, Int. J. Hyperthermia 36 (1) (2019) 517–528, https://doi.org/10.1080/02656736.2019.1605458.
[15] K.J.M. Surry, H.J.B. Austin, A. Fenster, T.M. Peters, Poly(vinyl alcohol) cryogel phantoms for use in ultrasound and MRI imaging, Phys. Med. Biol. 49 (24) (2004) 5529–5546, https://doi.org/10.1088/0031-9155/49/24/009.
[16] W. Xia, D. Piras, M. Heijblom, W. Steenbergen, T.G. van Leeuwen, S. Manohar, Poly(vinyl alcohol) gels as photoacoustic breast phantoms revisited, J. Biomed. Opt. 16 (7) (2011), 075002, https://doi.org/10.1117/1.3597616.
[17] G. Wojcik, T. Szabo, J. Mould, L. Carcione, F. Clougherty, Nonlinear pulse calculations and data in water and a tissue mimic, in: Proceedings of the IEEE Ultrasonics Symposium 2, 1999, pp. 1521–1526, https://doi.org/10.1109/ULTSYM.1999.849286.
[18] M. Earle, G. De Portu, E. De Vos, Agar ultrasound phantoms for low-cost training without refrigeration, Afr. J. Emerg. Med. 6 (1) (2016) 18–23, https://doi.org/10.1016/j.afjem.2015.09.003.
[19] E.L. Madsen, G.R. Frank, F. Dong, Liquid or solid ultrasonically tissue-mimicking materials with very low scatter, Ultrasound Med. Biol. 24 (4) (1998) 535–542, https://doi.org/10.1016/s0301-5629(98)00013-1.
[20] G. Menikou, M. Yiannakou, C. Yiallouras, C. Ioannides, C. Damianou, MRI-compatible breast/rib phantom for evaluating ultrasonic thermal exposures, Int. J. Med. Robot 14 (1) (2017), https://doi.org/10.1002/rcs.1849.
[21] G. Menikou, T. Dadakova, M. Pavlina, M. Bock, C. Damianou, MRI compatible head phantom for ultrasound surgery, Ultrasonics 57 (2015) 144–152, https://doi.org/10.1016/j.ultras.2014.11.004.
[22] R. Concalves, A.J. Trinca, G.C. dos Santos Ferreira, Effect of coupling media on velocity and attenuation of ultrasonic waves in Brazilian wood, J. Wood Sci. 57 (2011) 282–287, https://doi.org/10.1007/s10086-011-1177-y.
[23] H. Berndt, G.C. Johnson, Examination of wave propagation in wood from a microstructural perspective, Rev. Progr. Quant. Nondestruct. Eval. 14 (1995) 1661–1668, https://doi.org/10.1007/978-1-4615-1987-4_213.
[24] F. Liu, P. Xu, H. Zhang, C. Guan, D. Feng, X. Wang, Use of time-of-flight ultrasound to measure wave speed in poplar seedlings, Forests 10 (8) (2019) 17, https://doi.org/10.3390/f10080682.
[25] H. Sakai, K. Takagi, A. Minanisawa, Ultrasonic properties in woods, Jpn. J. Appl. Phys. 27 (1988) 55–57.
[26] E.Y. Sari, P. Nasution, F. Ramdhan, Characteristics of physical properties of wood powder composites and bagasseas construction materials of ship, SPERMONDE 5 (1) (2019) 11–15, https://doi.org/10.20956/jiks.v5i1.7038.
[27] B. Ababneh, A.A. Tajuddin, R. Hashim, I.L. Shuaib, S.M. Isa, A. AL-Jarrah, Evaluation of the relaxation times for Rhizophore app. Wood as human tissue equivalent for MRI breast phantom, Asian J. Appl. Sci. 3(6) (2015) 759–764.
[28] E.L. Madsen, M.A. Hobson, H. Shi, T. Varghese, G.R. Frank, Tissue-mimicking agar/gelatin materials for use in heterogeneous elastography phantoms, Phys. Med. Biol. 50 (23) (2005) 5597–5618, https://doi.org/10.1088/0031-9155/50/23/013.
[29] D. Nečas, P. Klapetek, Gwyddion: an open-source software for SPM data analysis, Cent. Eur. J. Phys. 10 (1) (2012) 181–188.
[30] E.L. Madsen, J.A. Zagzebski, G.R. Frank, Oil-in-gelatin dispersions for use as ultrasonically tissue-mimicking materials, Ultrasound Med. Biol. 8 (3) (1982) 277–287, https://doi.org/10.1016/0301-5629(82)90034-5.
[31] A. Keshavarzi, S. Vaezy, P.J. Kaczkowski, et al., Attenuation coefficient and sound speed in human myometrium and uterine fibroid tumors, J. Med. Ultrasound 20 (5) (2001) 473–480, https://doi.org/10.7863/jum.2001.20.5.473.
[32] T. Drakos, M. Giannakou, G. Menikou, C. Ioannides, C. Damianou, An improved method to estimate ultrasonic absorption in agar-based gel phantom using thermocouples and MR thermometry, Ultrasonics 103 (2020), 106089, https://doi.org/10.1016/j.ultras.2020.106089.
[33] G. Menikou, C. Damianou, Acoustic and thermal characterization of agar based phantoms used for evaluating focused ultrasound exposures, J. Ther. Ultrasound 5 (2017) 14, https://doi.org/10.1186/s40349-017-0093-z.
[34] A. Cafarelli, A. Verbeni, A. Poliziani, P. Dario, A. Menciassi, L. Ricotti, Tuning acoustic and mechanical properties of materials for ultrasound phantoms and smart substrates for cell cultures, Acta Biomater. 49 (2016) 368–378, https://doi.org/10.1016/j.actbio.2016.11.049.
[35] S. Mueller, L. Sandrin, Liver stiffness: a novel parameter for the diagnosis of liver disease, Hepat Med. 2 (2010) 49–67, https://doi.org/10.2147/hmer.s7394.
[36] A.E. Stewart, J. Rabinovici, M.C. Tempany, Y. Inbar, L. Regan, B. Gostout, Clinical outcomes of focused ultrasound surgery for the treatment of uterine fibroids, Fertil. Steril. 85 (1) (2006) 22–29, https://doi.org/10.1016/j.fertnstert.2005.04.072.
[37] A. Blana, B. Walter, S. Rogenhofer, F.W. Wieland, High-intensity focused ultrasound for the treatment of localized prostate cancer, Urology 63 (2) (2004) 297–300, https://doi.org/10.1016/j.urology.2003.09.020.
[38] J.W. Elias, D. Huss, T. Voss, J. Loomba, M. Khaled, E. Zadicario, A pilot study of focused ultrasound thalamotomy for essential tremor, N. Engl. J. Med. 369 (7) (2013) 640–648, https://doi.org/10.1056/NEJMoa1300962.
[39] A. P. Hasgall, F. Gennaro, C. Baumgartner, E. Neufeld, C.M. Gosselin, D. Payne, IT'IS Database for thermal and electromagnetic parameters of biological tissues, Version 2.6, www.itis.ethz.ch/database, 2015 (accessed 26 March 2020).
[40] Z. Bu-Lin, H. Bing, K. Sheng-Li, Y. Huang, W. Rong, L. Jia, A polyacrylamide gel phantom for radiofrequency ablation, Int. J. Hyperthermia 24 (7) (2008) 568–576, https://doi.org/10.1080/02656730802104732.
[41] C. Lafon, J.P. Kaczkowski, S. Vaezy, M. Noble, A.O. Sapozhnikov, Development and characterization of an innovative synthetic tissue-mimicking material for high intensity focused ultrasound (HIFU) exposures, in: IEEE Ultrasonics Symposium, Atlanta, 2001, https://doi.org/10.1109/ULTSYM.2001.991957.
[42] P.M. Robinson, J.M. Richardson, L.J. Green, W.A. Preece, New materials for dielectric simulation of tissues, Phys. Med. Biol. 36 (12) (1991) 1565–1571, https://doi.org/10.1088/0031-9155/36/12/002.
[43] P.C. Labuda, C.C. Church, Augmentation of HIFU-induced heating with fibers embedded in a phantom, Ultrasound Med. Biol. 37 (3) (2011) 442–449, https://doi.org/10.1016/j.ultrasmedbio.2010.12.010.
[44] J. Crezee, J.J. Lagendijk, Temperature uniformity during hyperthermia: the impact of large vessels, Phys. Med. Biol. 37 (6) (1992) 1321–1337, https://doi.org/10.1088/0031-9155/37/6/009.
[45] Y.C. Lai, E.D. Kruse, F.C. Caskey, N.D. Stephens, L.P. Sutcliffe, W.K. Ferrara, Noninvasive thermometry assisted by a dual-function ultrasound transducer for mild hyperthermia, IEEE Trans. Ultrason., Ferroelectr., Freq. Control 57 (12) (2010) 2671–2684, https://doi.org/10.1109/TUFFC.2010.1741.
[46] J. Blumm, A. Lindemann, Characterization of the thermophysical properties of molten polymers and liquids using the flash technique, High Temp. High Press. 35 (6) (2003) 627–632, https://doi.org/10.1118/1.595535.
[47] K. Giering, I. Lamprecht, O. Minet, Specific heat capacities of human and animal tissues, in: Proc. SPIE 2624, Laser-Tissue Interaction and Tissue Optics, 1996, https://doi.org/10.1117/12.229547.
[48] A.P. Bottomley, H.T. Foster, E.R. Argersinger, M.L. Pfeiffer, A review of normal tissue hydrogen NMR relaxation times and relaxation mechanisms from 1–100 MHz: dependence on tissue type, NMR frequency, temperature, species, excision and age, Med. Phys. 11 (4) (1984) 425–448, https://doi.org/10.1118/1.595535.

Received: 23 February 2021 | Revised: 21 May 2021 | Accepted: 21 May 2021

DOI: 10.1002/rcs.2287

ORIGINAL ARTICLE

The International Journal of Medical Robotics and Computer Assisted Surgery

WILEY

Simple methods to test the accuracy of MRgFUS robotic systems

Anastasia Antoniou[1] | Theocharis Drakos[2] | Marinos Giannakou[2] | Nikolas Evripidou[1] | Leonidas Georgiou[3] | Theodora Christodoulou[3] | Natalie Panayiotou[3] | Cleanthis Ioannides[3] | Nikolaos Zamboglou[3] | Christakis Damianou[1]

[1]Department of Electrical Engineering, Computer Engineering, and Informatics, Cyprus University of Technology, Limassol, Cyprus

[2]R&D, Medsonic LTD, Limassol, Cyprus

[3]German Oncology Center, Limassol, Cyprus

Correspondence
Christakis Damianou, Department of Electrical Engineering, Computer Engineering, and Informatics, Cyprus University of Technology, 30 Archbishop Kyprianou St, Limassol 3036, Cyprus.
Email: christakis.damianou@cut.ac.cy

Funding information
Research and Innovation Foundation of Cyprus, Grant/Award Numbers: ENTERPRISES/0618/0016, ENTERPRISES/0918/0012, INTEGRATED/0918/0008

Abstract

Background: Robotic-assisted diagnostic and therapeutic modalities require a highly accurate performance to be certified for clinical application. In this paper, three simple methods for assessing the accuracy of motion of magnetic resonance-guided focused ultrasound (MRgFUS) robotic systems are presented.

Methods: The accuracy of motion of a 4 degrees of freedom robotic system intended for preclinical use of MRgFUS was evaluated by calliper-based and magnetic resonance imaging (MRI) methods, as well as visually by performing multiple ablations on a plastic film.

Results: The benchtop results confirmed a highly accurate motion in all axes of operation. The spatial positioning errors estimated by MRI evaluation were defined by the size of the imaging pixels. Lesions arrangement in discrete and overlapping patterns confirmed satisfactory alignment of motion trajectories.

Conclusions: We believe the methods presented here should serve as a standard for evaluating the accuracy of motion of MRgFUS robotic systems.

KEYWORDS
motion accuracy, MRgFUS robotic devices, simple evaluation methods

1 | INTRODUCTION

The introduction of robots in medicine has been essential for establishing minimally invasive diagnostic and therapeutic modalities by extending their benefits to most surgical specialties.[1] Robotic devices are continuously being invented to aid in the positioning and manipulation of surgical instruments and energy sources. Such robotic-assisted procedures require a highly accurate operation to approach a target in a minimally invasive manner and meet the clinical requirement. Simultaneously, the accuracy data are essential for establishing safety guidelines for clinical applications.

All the techniques used to test the mechanical accuracy of a robot are based on the idea of comparing the commanded motion step with the actual displacement as estimated by a distance-measuring technique. Mechanical accuracy refers to both the positioning and repeatability accuracy of motion. Before the procedure is applied and evaluated in vivo, accuracy assessment is typically carried out in free space, sometimes referred to as intrinsic system accuracy, meaning not under real conditions. Most commonly, after acquiring evidence of

sufficient accuracy and repeatability by benchtop testing, the system is evaluated in the environment that is intended to be clinically used, such as the bore of a magnetic resonance imaging (MRI) system. This is essential for ensuring that the system maintains a high degree of accuracy in real-like scenarios. Even a minimal magnetic shift of the system's components in the MRI could affect the accuracy and compromise the patient's safety in highly sensitive procedures.

Regarding benchtop evaluation, several motion-tracking techniques were proposed for assessing the accuracy of motion in a free robot workspace.[2–7] Optical tracking systems have been widely used for confirming adequate targeting accuracy for needle-related interventions, where the placement error is defined by the deviation of the actual tooltip position from the desired location.[2–5] The accuracy of an automated robot intended for breast biopsy in precisely reaching a target was evaluated using a rigid test tool, which was driven to target positions through straight and angled paths and monitored with an optical tracker.[2] Similarly, Patriciu et al.[3] investigated the motion accuracy of a system for automated brachytherapy seed placement using an optical tracking system. An active marker was mounted on the end-effector of the robotic arm allowing continuous tracking of its position. An optical tracking system was also used by Patel et al.[4] who evaluated a robotic system intended to perform shoulder arthrography. A specially designed frame with optical markers served as the reference, while a tracking structure was also integrated on the needle guide so that its position can be tracked relative to the reference frame.[4] A different tracking method was chosen by Dou et al.[5] who measured the positioning accuracy of a brachytherapy system using a 3D laser tracker, as well as an inertial measurement unit.[5] An optical measuring microscope has also been proposed for estimating the actual displacement of a linear motion stage after the execution of commanded movements of varying distance.[6] In another study,[7] the displacement of an endoscope manipulator was measured with two charge-coupled device laser micrometres.

More straightforward methods involving the use of digital callipers and special structures have also been carried out in the laboratory environment for accuracy evaluation purposes. The needle tip accuracy of a breast biopsy robot was evaluated in free air by targeting crosshairs drawn on a board.[8] The needle tip was commanded to puncture these targets, and the error was estimated by the distance from the centre of each target to the corresponding pierced hole.[8] Similarly, in the framework of evaluating the motion accuracy of a robot intended for transcranial focussed ultrasound (FUS) surgery, the FUS transducer was replaced by a felt-tipped pen, which was commanded to touch multiple resolution points distributed on three perpendicular planes demonstrating the entire robot's workplace.[9] Each created mark was assigned in resolution circles having radial and angular approximation zones for facilitating targeting error measurement.[9] Another simplified method involves mounting digital callipers on the motion stages of a robot such that their actual displacement after motion execution can be directly measured by the incremental distance of the calliper.[10,11]

After assessing the accuracy of needle-related interventions in free space, experiments under more realistic conditions are typically performed. Initial experiments are predominantly performed in phantoms in an imaging environment, involving the use of fiducial markers for visualizing and registering the system in the imaging coordinates. A first planning scan is typically acquired for selecting the target locations in the phantom and calculating the insertion parameters.[12–14] Following targeting according to the estimated coordinates exported to a motor controller software, confirmation images are collected for assessing the accuracy of needle placement relative to the prescribed locations.[12–14] In a phantom study performed by Patel et al.[12] under real-time MRI guidance, a needle-based therapeutic ultrasound applicator was robotically inserted in a gelatine phantom in locations predefined in 3D slicer. The intended probe tip position was compared to the actual position as visualized in 3D-fast field echo images. Likewise, Krieger et al.[13] assessed the accuracy of motion of a system for prostate interventions in a tissue-mimicking phantom. The rectal sheath was automatically aligned with the desired insertion point and then manually inserted in the phantom. The void caused by the needle tip was visualized in axial turbo spin echo proton density images enabling calculation of the in-plane error of targeting.[13] Targeting accuracy assessment in MRI was also performed in air with the use of a gadolinium filled virtual needle, which was tracked and visualized using T1-weighted Isotropic Volume Examination sequence.[14]

Robotic devices intended for non-invasive FUS applications are constantly being developed[15] and extensively evaluated by performing ablation studies, in which the separation precision of multiple ablations constitutes an indication of the positioning error. Tao Wu et al.[16] performed quality control of a FUS system, where the focus positioning accuracy was tested by performing multiple sonications on a Lucite cart. The transducer was accommodated in a water tank to be acoustically coupled to the target. Left-right and superior-inferior movements by specific distance were commanded by a treatment planning software, resulting in numerous sets of melted spots arranged in discrete patterns. The actual distance between adjacent spots was measured with a digital calliper.[16] In other phantom experiments conducted in a benchtop setting,[10] the linear motion stages were commanded to create discrete ablations of specific spacing in a gel phantom. White coagulation lesions were clearly visible, being spaced by the desired step, thus confirming the accuracy of positioning.

Price et al.[9] followed a similar approach but in an MRI setting. An MR conditional robot for transcranial FUS interventions was used to perform multiple sonications in a 2×3 pattern in a heat-sensitive gel phantom located in a water tank. The thermal images acquired after each sonication were superimposed onto one image, and the positioning accuracy was defined as the spacing between the centres of adjacent ablated areas.[9] This technique was also selected for evaluating the accuracy of motion of an MR-compatible FUS device intended for brain diseases treatment.[17] A four-point ablation pattern was performed in vitro, in lamb brain, with different motion steps of 1–10 mm, and the formed lesions were visualized in T1-weighted fast spin echo (FSE) images. The ablated areas appeared as spots of increased signal intensity, and the distance between neighbouring ablations was calculated from the centre of each spot. Notably, smaller errors were estimated with increasing step

distance.[17] Similarly, Yiallouras et al.[11] performed phantom experiments where T2-weighted FSE images revealed areas of reduced signal formed in a discrete pattern. It is notable that Sagias et al.[18] developed a motion phantom for evaluating FUS protocols specifically for moving targets in the MRI environment. In another study carried out in a gel phantom,[19] the robotic arm of an US-guided FUS ablation system was commanded to move the focal point to ablate the four corners of the phantom, and the targeting accuracy was assessed by visualizing the sonicated areas on US images.

Herein, we present three simple methods that were used for assessing the accuracy of motion of a magnetic resonance-guided focused ultrasound (MRgFUS) robotic system in both benchtop and MRI environments. The system is intended for ex vivo and in vivo preclinical use, including studies in companion animals of all sizes with naturally occurring tumours. In the first method, a digital calliper is mounted on the motion stage under evaluation with the assistance of specially designed 3D-printed parts, having its one edge fixed on a stationary part and the other on a movable part. In that way, a specific step movement of the stage results in an analogous increment in the calliper. The second evaluation procedure relates to accuracy assessment in the MRI setting. The robotic device is sited on the MRI couch, and a plastic marker is mounted on the top of the FUS transducer so that it can be visualized in MR images. The third method involves performing multiple ablations in a transparent plastic film by robotic movement of the transducer.

2 | MATERIALS AND METHODS

2.1 | Robotic system

A robotic system featuring 4 degrees of freedom (DOF) was developed to be used in the preclinical setting for ex vivo and in vivo applications of the MRgFUS technology. It is particularly intended to treat cancer in small and large companion animals with naturally occurring tumours.

The positioning device was designed (Inventor Professional 2018; Autodesk) and 3D-printed (F270; Stratasys Ltd.) with acrylonitrile butadiene styrene thermoplastic material. Some of the design criteria included reduction of the total size of the device as much as possible while maintaining sufficient motion range. This compact design allows for easy incorporation of the device in the table of any conventional MRI scanner. A specially designed mattress is adapted around the protruding part of the device to raise the table to the exact height of the device.

The positioning mechanism features motion in 4 DOF, which is adequate to ablate a tissue volume of any shape and size. Specifically, the device allows the user to linearly navigate the focussed transducer in three axes (*X*, *Y* and *Z*), whereas angular rotation about a single axis is also available. The *X* and *Y* motion stages allow movement in two orthogonal horizontal axes, while the *Z* stage provides motion in a vertical axis. Accordingly, the Θ stage enables rotation of the transducer about its shaft. All motion stages are computer-controlled through a customized software. Due to the constrain of the MRI bore, there are some spatial limits, and therefore, motion restrictions. The maximum travel of the transducer is 60 mm in the *X* axis (forward and reverse), 75 mm in the *Y* axis (left and right) and 26 mm in the *Z* axis (up and down). The rotation limit is 90°: 45° clockwise (CW) and 45° counter-clockwise (CCW). Piezoelectric motors (USR60-S3; Shinsei Corporation) and dual digital encoders (US Digital Corporation) were incorporated in all motion stages, thus providing a highly accurate motion. More precisely, the system is characterized by a high resolution of 500 lines per inch for the linear strip and 2500 lines for a full rotation of the plastic disk. The computer-aided design (CAD) drawing of the fully assembled robotic device is shown in Figure 1.

2.2 | Digital callipers method

The motion accuracy of the positioning mechanism was evaluated using digital callipers with a measuring accuracy of 0.01 mm. The digital callipers (one for the linear stages and one for the angular stage) were mounted and stabilized on 3D-printed structures. The structures were easily attached to the robotic device, as illustrated in Figure 2. In that way, the calliper was perfectly aligned with the axis under evaluation, thus providing accurate distance estimation. The one edge of the calliper was securely mounted on a stationary part of

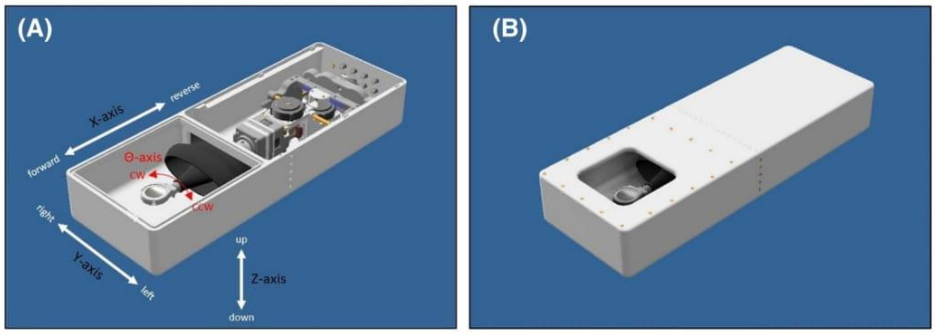

FIGURE 1 Computer-aided design drawing of the 4 degrees of freedom robotic system (A) without the cover (components are visualized) and (B) with the cover

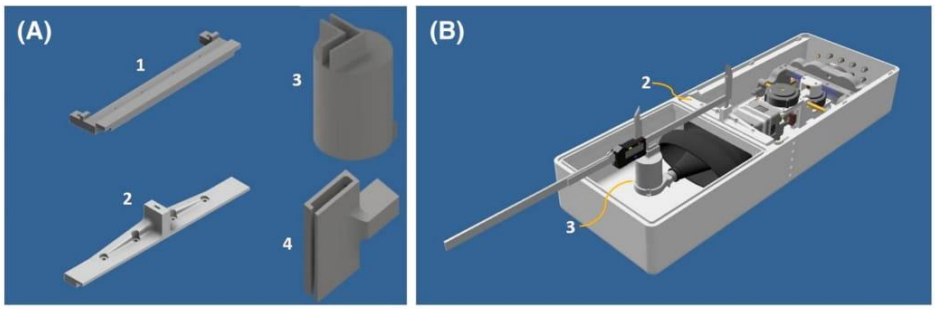

FIGURE 2 (A) Stationary (1, 2, 4) and moveable (3) 3D-printed structures that were used for the *X* and *Y* axes distance measurements and (B) computer-aided design drawing of the setup that was used for the *X* axis motion accuracy estimation

the device, while the other part was attached to the movable part (Figure 2). A different structure was used for the measurement of the angular motion, as shown in Figure 3. Note that this stage was evaluated separately, outside of the mechanism enclosure. In each case, the motion stage was moved through the designed software at a certain distance (or degrees), and the actual displacement was measured by the incremental distance in the calliper. Both directions of each linear axis were evaluated at step movements of 1, 5 and 10 mm. Accordingly, the angular motion accuracy was evaluated for CW and CCW directions at step angles of 1°, 5° and 10°.

Moreover, the speed of motion of the robotic device in all axes (*X*, *Y*, *Z* and Θ) and directions was calculated by the time required for the stage to cover specific step movements, which was equal to the activation time of the piezoelectric motors as provided by the software.

2.3 | MRI method

Another simple method for estimating the motion accuracy of a robotic system is through MRI. This method is limited to MR-compatible robotic devices. The concept of the proposed technique is based on the fact that structures without protons appear dark in MR images. The focused transducer was replaced by a 3D-printed plastic structure with a tip of 2 mm thickness, which served as a marker, and the water enclosure was filled with degassed water. The robotic device was placed inside an MRI scanner (1.5 T, GE Signa HD16; General Electric Healthcare) and covered with a Signa 1.5 T General Purpose flex surface coil (General Electric Medical Systems). Figure 4A illustrates the experimental setup as placed on the MRI table, while Figure 4B shows a CAD drawing of the plastic marker. MR scanning was performed using an FSE sequence in coronal plane. The main MRI parameters were: repetition time = 800 ms, echo time = 19 ms, flip angle = 90°, echo train length = 3, pixel bandwidth = 65.1 and field of view = 280 × 280 × 10 mm^3.

The accuracy of linear motion was assessed in the *X* and *Y* axes. The initial position of the tip was located, and then the transducer was moved by a certain distance. Bidirectional movements with a step of 3 and 5 mm in both axes were tested. An MR image was acquired after each step movement to detect the tip location. A special approach was followed for locating the position of the 2 mm thick tip of the plastic marker. First, the image zoom was enhanced to focus on the plastic marker. Then, the corresponding pixels were scanned to identify the *x* and *y* coordinates of the pixel with the lowest signal intensity (this was assumed to be the centre of the marker in the image). The change in pixel number after a step movement reflected the shift in position of the transducer in the tested direction. The pixel difference was then multiplied by the pixel size (0.5469 mm) of the acquisition matrix so as to measure the shift in millimetres. This technique had an inherent error of ±1 pixel, which translated to ±0.5469 mm. Finally, the series of images were superimposed onto one image for visualizing the motion patterns.

2.4 | Visual method

The motion accuracy was also assessed through visual observations of multiple ablations produced on a transparent plastic film (0.9 mm thickness, FDM400mc print plate; Stratasys Ltd.). The acoustic attenuation of the plastic film at the frequency of 2.1 MHz was 8.5 ± 0.2 dB/cm-MHz based on a standard transmission through immersion technique.[20] The water enclosure containing the transducer (spherically focused, frequency: 1.1 MHz, diameter: 50 mm, focal length: 70 mm; Medsonic Ltd.) was filled with degassed water up to the plastic film. The robotic device was moved to sonicate the film in square grid patterns for evaluating the accuracy of motion, as well as the linear motion alignment in the *X* and *Y* axes. An acoustic power of 10 W was applied at each grid point using an RF amplifier (AG1012; T & C Power Conversion, Inc.). The sonication time varied from 1–4 s so as to control the lesion size. Subsequently, sonications were performed with varying motion step and sonication time, with the time delay between the successive sonications set at 30 s. Also, the maximum motion range of the positioning mechanism in the horizontal plane was estimated by applying sonications at the extreme points of movement in the *X* and *Y* axes. It is noted that lesion formation was a result of reflection from the plastic/air interface.

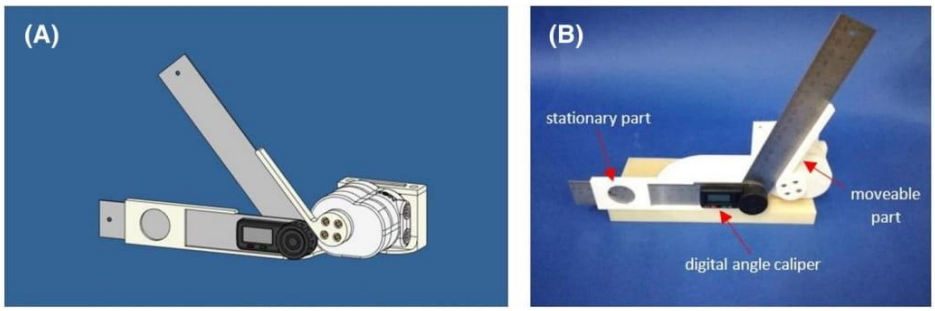

FIGURE 3 Experimental setup used for estimating the angular motion accuracy using the digital angle calliper; (A) computer-aided design drawing and (B) photo

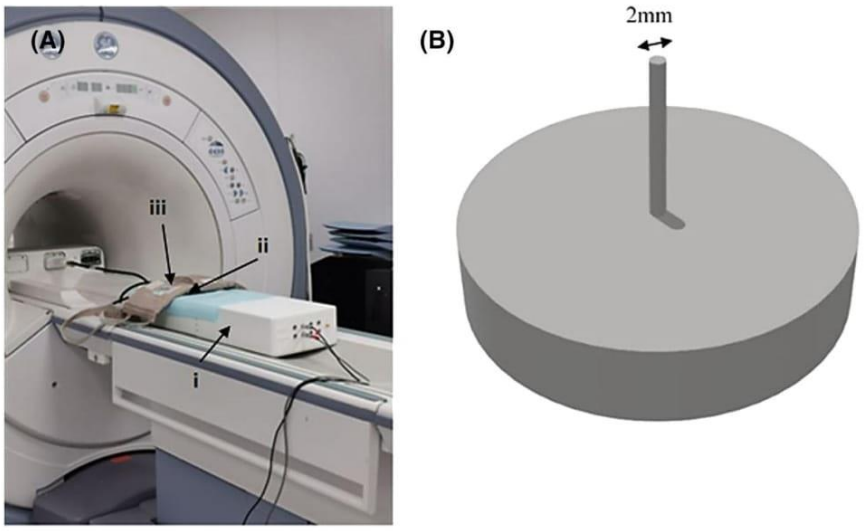

FIGURE 4 (A) The robotic device (i) as placed on the magnetic resonance imaging table, showing the location of the plastic marker (ii) and the flex surface coil (iii), and (B) computer-aided design drawing of the plastic marker used for accuracy measurements

3 | RESULTS

The motion accuracy of the robotic device in both linear and angular axes was evaluated using digital callipers. Linear motion steps of 1, 5 and 10 mm and angular steps of 1°, 5° and 10° were performed for 20 repetitions in bidirectional movements. Figure 5 shows a bar chart that displays the actual distance measured at a commanded step movement of 5 mm in both *X* axis directions for each repetition measurement. The range of actual displacement measured at each commanded step, as well as the mean motion error and standard deviation for all the axes (*X*, *Y*, *Z* and Θ) are listed in Table 1. Furthermore, the speed of motion of all stages in bidirectional movements was calculated according to the motors' activation time during movement execution. The corresponding results are also listed in Table 1.

MRI was also used to examine the accuracy of motion in the *X* and *Y* axes. The MR images acquired after execution of each 3 mm motion step in the *X* axis reverse and *Y* axis right directions were superimposed onto the images shown in Figure 6A,B, respectively. Table 2 lists the range of actual distance measured for each commanded motion step (3 and 5 mm) and each direction, as well as the corresponding mean motion error and standard deviation.

The motion accuracy was visually observed by sonicating plastic films. Sonications at the extreme points of movement in the horizontal plane revealed a maximum motion range equal to 6 and 7 cm in the *X* and *Y* axes, respectively. The effect of lesion formation on the plastic film was originally examined by varying the sonication time while keeping constant the acoustic power as shown in Figure 7. The appropriate selection of sonication time and grid step allowed formation of discrete and overlapping lesions and visual evaluation of the accuracy of motion and alignment. Figure 8 shows discrete lesions formed after applying sonications at acoustical power of 10 W for 1 s, in a 6 × 5 grid pattern with a step distance of 5 mm. The formed lesions show satisfactory alignment in both axes. Sonications at the same acoustical power for a longer time of 3 s in a 15 × 15 grid pattern with the same time delay of 30 s, but a smaller spatial step of 2 mm, resulted in overlapping lesions as illustrated in Figure 9. The ablated area was well defined in a square of about 3.3 × 3.3 cm^2, without any significant protrusions.

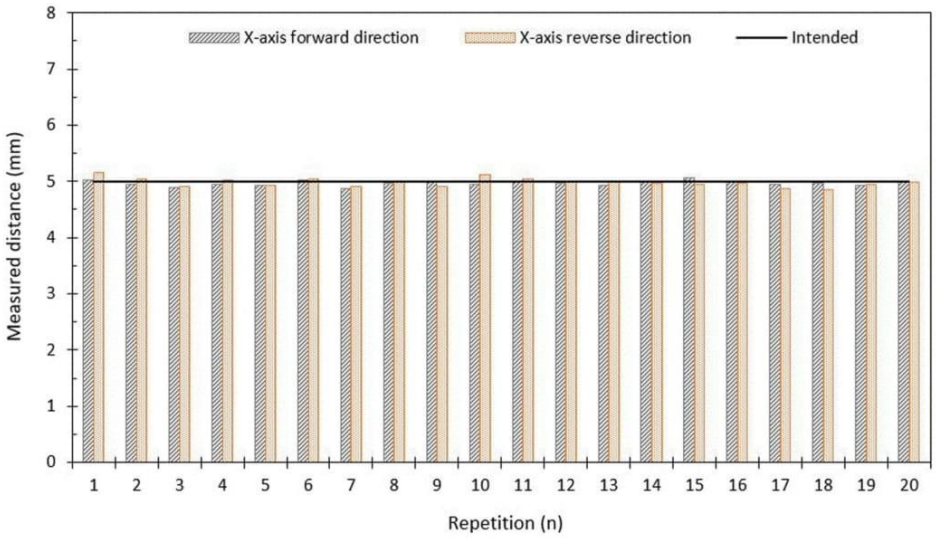

FIGURE 5 Distance measurements for 20 repetitions in the *X*-axis with step movement of 5 mm in bidirectional movements. The black straight line indicates the commanded distance

4 | DISCUSSION

In this paper, three simple and practical methods for assessing the accuracy of motion of a robotic device are described. It is emphasized that the calliper and MRI methods are suitable for evaluating any robotic system, while ablation of the plastic film is intended specifically for FUS systems. It is also noted that the device should be MR-compatible in order to be properly evaluated in an MRI environment. All these methods are based on the idea of evaluating the performance of the device in accurately executing commanded movements.

First, the motion accuracy of an MRgFUS robotic device was evaluated using digital callipers integrated on the motion stages under evaluation using specially designed 3D-printed structures. The mean error of linear motion varied from 0.042 ± 0.032 mm for the 1 mm step in the *X* axis forward direction to 0.123 ± 0.082 mm for the 10 mm step in the *Y* axis right direction. Accordingly, the mean error of angular motion varied from a minimum value of 0.100 ± 0.077° for the 1° step to a maximum value of 0.320 ± 0.225° for the 10° step (CW rotation). Contrary to the findings of a previous study,[17] the mean error was found to be increasing with increasing motion step for all four axes.

The speed of motion was estimated by the time activation of the robot's motors as provided by the controlling software during motion execution. The results revealed no significant difference in speed of motion for bidirectional movements. A mean motion speed of approximately 10 mm/s was estimated for both the *X* and *Z* axes, while a higher value of about 14 mm/s was found for the *Y* axis.

In comparison with previous designs,[10,11,17,21] the principle of movement of the proposed one was significantly improved by the dual encoder positioning control that guarantees a smooth, reliable and highly accurate motion in all stages. Additionally, the problem of reduced accuracy for small steps previously observed[17] seems to be solved by using faster software commands that makes the encoder's reading more accurate.

The system was then evaluated in the MRI environment that is intended to be used. The accuracy of motion remains satisfactory during full operation of the system in the MRI environment. Additionally, there was no evidence of any magnetically induced shift of the mechanical components that could compromise the accuracy of ultrasound delivery to the target, and therefore the patient's safety.

The spatial positioning errors estimated by the benchtop setting using digital callipers are significantly smaller than those obtained in the MRI setting. This is attributed to the size of voxels of the MR images that determine the finest possible accuracy. Given the MRI resolution of about 0.55 mm per pixel, the estimated motion errors are within a reasonable range. Although this approach suffers from imaging resolution limitations, a smaller pixel could provide more precise distance estimates, but at the cost of increased image acquisition time and reduced signal to noise ratio.

The high degree of accuracy evidenced by benchtop testing with callipers was also confirmed by multiple ablations on a transparent plastic film. The melted spots formed after grid ablation were arranged in a discrete pattern, in a highly accurate manner, clearly demonstrating that the linear stages were moved by the commanded step. As observed, the centres of almost all the spots were equally spaced, demonstrating excellent repeatability. Multiple ablations in a grid with a smaller spatial step between adjacent sonications and three times longer sonication time resulted in a well-defined square area of overlapping lesion. The results suggest that the system can precisely ablate a large tissue volume by overlapping lesions.

The aforementioned ablation method is intended specifically for testing the accuracy of FUS systems and is essential for assessing

TABLE 1 The range of distance measurements as estimated by the digital callipers at commanded spatial steps of 1, 5 and 10 mm in each linear axis and angular step of 1°, 5°, and 10° about the rotational axis, the corresponding mean motion error and standard deviation and the mean speed and standard deviation in each case

Linear axis	Commanded step (mm)	Range of actual displacement (mm)	Mean error ± SD forward (mm)	Mean error ± SD reverse (mm)	Mean speed ± SD forward (mm/s)	Mean speed ± SD reverse (mm/s)
X	1	0.88–1.08	0.042 ± 0.032	0.051 ± 0.032	10.31 ± 0.62	10.05 ± 0.26
	5	4.85–5.15	0.047 ± 0.033	0.065 ± 0.044	10.43 ± 0.57	9.80 ± 0.94
	10	9.78–10.19	0.081 ± 0.058	0.058 ± 0.057	10.01 ± 0.21	9.98 ± 0.78
Y	**Commanded step (mm)**	**Range (mm)**	**Error right (mm)**	**Error left (mm)**	**Speed right (mm/s)**	**Speed left (mm/s)**
	1	0.88–1.09	0.045 ± 0.042	0.042 ± 0.026	14.28 ± 1.40	15.93 ± 0.83
	5	4.89–5.19	0.053 ± 0.032	0.084 ± 0.050	13.84 ± 1.02	14.16 ± 0.62
	10	9.85–10.29	0.123 ± 0.082	0.086 ± 0.061	14.66 ± 0.29	14.46 ± 0.64
Z	**Commanded step (mm)**	**Range (mm)**	**Error up (mm)**	**Error down (mm)**	**Speed up (mm/s)**	**Speed down (mm/s)**
	1	0.89–1.11	0.052 ± 0.029	0.039 ± 0.030	9.90 ± 0.20	10.09 ± 0.21
	5	4.90–5.11	0.055 ± 0.037	0.055 ± 0.035	9.90 ± 0.13	9.73 ± 0.30
	10	9.78–10.11	0.069 ± 0.060	0.084 ± 0.062	9.78 ± 0.08	9.59 ± 0.38
Angular axis	**Commanded step (°)**	**Range (°)**	**Error CW (°)**	**Error CCW (°)**	**Speed CW (°/s)**	**Speed CCW (°/s)**
Θ	1	0.8–1.3	0.100 ± 0.077	0.155 ± 0.097	132.4 ± 12.2	118.8 ± 16.2
	5	4.7–5.7	0.250 ± 0.175	0.245 ± 0.193	144.5 ± 10.8	145.1 ± 10.2
	10	9.9–10.7	0.320 ± 0.225	0.290 ± 0.251	148.4 ± 3.74	144.5 ± 3.2

Abbreviations: CW, clockwise; CCW, counter-lockwise.

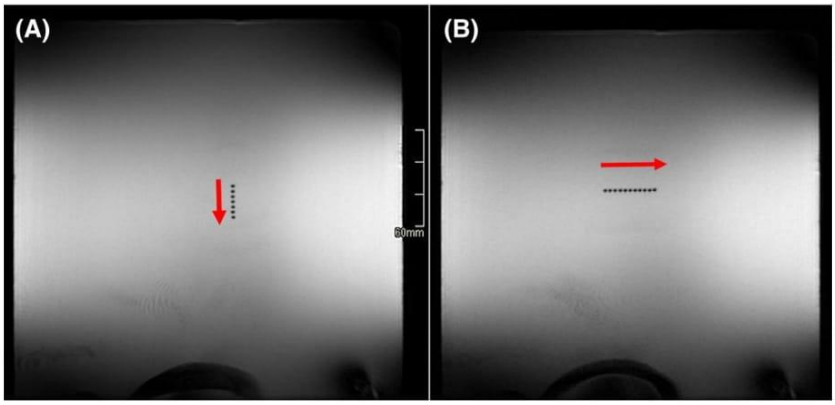

FIGURE 6 Minimum intensity projection from a combination of fast spin echo coronal images that shows a (A) reverse step movement of 3 mm in the *X* direction and (B) right step movement of 3 mm in the *Y* direction

TABLE 2 The range of distance measurements as estimated by MRI at commanded spatial steps of 3 and 5 mm in *X* and *Y* axes bidirectional movements, and the corresponding mean motion error and standard deviation

Linear axis	Commanded step (mm)	Range of actual displacement (mm)	Mean error ± SD forward (mm)	Mean error ± SD reverse (mm)
X	3	2.73–3.83	0.277 ± 0.007	0.342 ± 0.172
	5	4.92–5.47	0.339 ± 0.184	0.352 ± 0.179
	Commanded step (mm)	**Range of actual displacement (mm)**	**Mean error ± SD right (mm)**	**Mean error ± SD left (mm)**
Y	3	2.73–3.83	0.330 ± 0.166	0.278 ± 0.007
	5	4.37–5.47	0.171 ± 0.191	0.286 ± 0.239

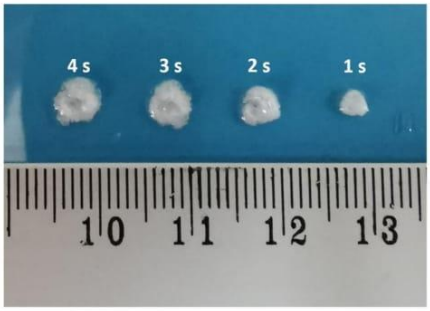

FIGURE 7 Effect of varying sonication time on lesion formation on the plastic film, using low power and a spatial step of 10 mm (transducer specifications: 1.1 MHz frequency, 50 mm diameter and 70 mm focal length)

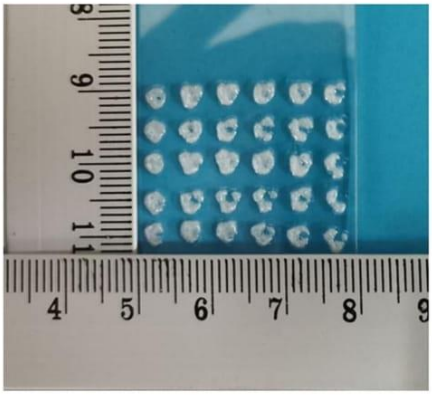

FIGURE 8 Discrete lesions as formed on the plastic film for sonications in a 6 × 5 grid pattern, with acoustical power of 10 W for 1 s and a step distance of 5 mm

their ability to precisely deliver heating spots along the desired pattern. It is notable that in such systems, the accuracy in free robot workspace is representative of that in more realistic scenarios (phantom and in vivo experiments), whereas, for instance, in needle-based interventions is not. This is consistent with what has been previously reported by Price et al.,[9] who found that the intrinsic accuracy of a FUS system as estimated in the air was similar to that obtained by phantom experiments in the MRI setting.

The proposed methods were greatly improved in terms of accuracy compared to those we have previously used.[10,11,22,23] The quality of benchtop evaluation was enhanced by using 3D-printed structures specially designed for each individual axis, which provided perfect alignment of the calliper with each axis of measurement and reduced systematic errors.[10] Regarding the MRI evaluation, the accuracy of step movement has been previously estimated by locating the transducer on MR images.[23] Advantageously, a more accurate method is proposed herein, involving the use of a 2 mm plastic marker, which is clearly visible on MRI images using the appropriate sequence.

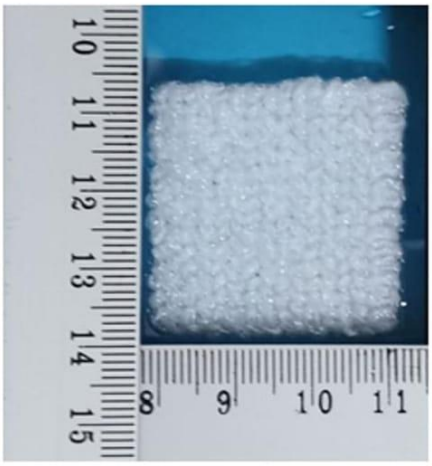

FIGURE 9 Overlapping lesions as formed on the plastic film for sonications in a 15 × 15 grid pattern, with acoustical power of 10 W for 3 s and a step distance of 2 mm

Overall, the accuracy of the tested robotic device, as proven from all three methods, is sufficient to guarantee an efficient performance of the system in terms of precise ablation in both laboratory and MRI environments. We believe the proposed methods should serve as the standard methods for evaluating FUS robotic systems.

ACKNOWLEDGEMENTS

The project was funded by the Research and Innovation Foundation of Cyprus under the projects: FUSROBOT (ENTERPRISES/0618/0016), PROSTASONIC (ENTERPRISES/0918/0012) and SOUNDPET (INTEGRATED/0918/0008).

CONFLICT OF INTERESTS

All declare no conflict of interest.

AUTHOR CONTRIBUTION

Anastasia Antoniou contributed in the drafting of the manuscript. Theocharis Drakos contributed in the benchtop evaluation of the motion accuracy of the robotic system and drafting of the manuscript. Marinos Giannakou contributed in the development of the robotic system. Nikolas Evripidou contributed in the development of the electronic system and 3D-printed structures. Leonidas Georgiou contributed in the MRI experiments. Theodora Christodoulou contributed in the MRI experiments. Natalie Panayiotou contributed in the MRI experiments. Cleanthis Ioannides contributed in the MRI experiments. Nikolaos Zamboglou contributed in the MRI experiments. Christakis Damianou served as the scientific coordinator and supervised the development of the system, implementation of the experiments and drafting of the manuscript.

DATA AVAILABILITY STATEMENT

The data that support the findings of this study are available from the corresponding author upon reasonable request.

ORCID

Marinos Giannakou https://orcid.org/0000-0002-6777-0515
Nikolas Evripidou https://orcid.org/0000-0002-8200-3349
Christakis Damianou https://orcid.org/0000-0003-0424-2851

REFERENCES

1. Peters BS, Armijo PR, Krause C, Choudhury SA, Oleynikov D. Review of emerging surgical robotic technology. *Surg Endosc*. 2018;32(4):1636-1655. https://doi.org/10.1007/s00464-018-6079-2
2. Chan KG, Fielding T, Anvari M. An image-guided automated robot for MRI breast biopsy. *Int J Med Robot Comput Assist Surg*. 2016;12(3):461-477. https://doi.org/10.1002/rcs
3. Patriciu A, Petrisor D, Muntener M, Mazilu D, Schär M, Stoianovici D. Automatic brachytherapy seed placement under MRI guidance. *IEEE Trans Biomed Eng*. 2007;54(8):1499-1506. https://doi.org/10.1109/TBME.2007.900816
4. Patel N, Yan J, Monfaredi R, Sharma K, Cleary K, Iordachita I. Pre-clinical evaluation of an integrated robotic system for magnetic resonance imaging guided shoulder arthrography. *Med Imaging*. 2019;6(2):1. https://doi.org/10.1117/1.JMI.6.2.025006
5. Dou H, Jiang S, Yang Z, Sun L, Ma X, Huo B. Design and validation of a CT-guided robotic system for lung cancer brachytherapy. *Med Phys*. 2017;44(9):4828-4837. https://doi.org/10.1002/mp.12435
6. Tavallaei MA, Johnson PM, Liu J, Drangova M. Design and evaluation of an MRI-compatible linear motion stage. *Med Phys*. 2016;43(1):62-71. https://doi.org/10.1118/1.4937780
7. Koseki Y, Washio T, Chinzei K, Iseki H. Endoscope Manipulator for Trans-nasal Neurosurgery, Optimized for and Compatible to Vertical Field Open MRI. In: International Conference on Medical Image Computing and Computer-Assisted Intervention—MICCAI 2002 Lect Notes Comput Sci; Springer, Berlin, Heidelberg. 2002, pp. 114-121.
8. Groenhuis V, Siepel FJ, Veltman J, van Zandwijk JK, Stramigioli S. Stormram 4: an MR safe robotic system for breast biopsy. *Ann Biomed Eng*. 2018;46(10):1686-1696. https://doi.org/10.1007/s10439-018-2051-5
9. Price KD, Sin VW, Mougenot C, et al. Design and validation of an MR-conditional robot for transcranial focused ultrasound surgery in infants. *Med Phys*. 2016;43(9):4983-4995. https://doi.org/10.1118/1.4955174
10. Yiallouras C, Mylonas N, Damianou C. MRI-compatible positioning device for guiding a focused ultrasound system for transrectal treatment of prostate cancer. *Int J Comput Assist Radiol Surg*. 2014;9(4):745-753. https://doi.org/10.1007/s11548-013-0964-x
11. Yiallouras C, Ioannides K, Dadakova T, Pavlina M, Bock M, Damianou C. Three-axis MR-conditional robot for high-intensity focused ultrasound for treating prostate diseases transrectally. *J Ther Ultrasound*. 2015;3(1):1-10. https://doi.org/10.1186/s40349-014-0023-2
12. Patel NA, Nycz CJ, Carvalho PA, et al. An integrated robotic system for MRI-guided neuroablation: preclinical evaluation. *IEEE Trans Biomed Eng*. 2020;67(10):2990-2999.
13. Krieger A, Song S-E, Cho NB, et al. Development and evaluation of an actuated MRI-compatible robotic system for MRI-guided prostate intervention. *IEEE ASME Trans Mechatron*. 2013;18(1):273-284. https://doi.org/10.1109/TMECH.2011.2163523
14. Moreau-gaudry JGA, Hungr N, Moreau-gaudry A, et al. Evaluation of the needle positioning accuracy of a light puncture robot under MRI guidance: results of a clinical trial on healthy volunteers. *Cardiovasc Intervent Radiol*. 2018;41(9):1428-1435. https://doi.org/10.1007/s00270-018-2001-5
15. Yiallouras C, Damianou C. Review of MRI positioning devices for guiding focused ultrasound systems. *Int J Med Robot Comput Assist Surg*. 2015;11:247-255. https://doi.org/10.1002/rcs.1601

16. Wu T. A quality control program for MR-guided focused ultrasound ablation therapy. *J Appl Clin Med Phys*. 2002;3(2):162. https://doi.org/10.1120/1.1459262
17. Mylonas N, Damianou C. MR compatible positioning device for guiding a focused ultrasound system for the treatment of brain diseases. *Int J Med Robot Comput Assist Surg*. 2014;10:1-10.
18. Sagias G, Yiallouras C, Ioannides K, Damianou C. An MRI-conditional motion phantom for the evaluation of high-intensity focused ultrasound protocols. *Int J Med Robot Comput Assist Surg*. 2016;12:431-441.
19. An CY, Syu JH, Tseng CS, Chang CJ. An ultrasound imaging-guided robotic HIFU ablation experimental system and accuracy evaluations. *Appl Bionics Biomech*. 2017;2017:1-8. https://doi.org/10.1155/2017/5868695
20. Menikou G, Damianou C. Acoustic and thermal characterization of agar based phantoms used for evaluating focused ultrasound exposures. *J Ther Ultrasound*. 2017;5:1-14. https://doi.org/10.1186/s40349-017-0093-z
21. Damianou C, Ioannides K, Milonas N. Positioning device for MRI-guided high intensity focused ultrasound system. *Int J Comput Assist Radiol Surg*. 2008;2(6):335-345. https://doi.org/10.1007/s11548-007-0145-x
22. Epaminonda E, Drakos T, Kalogirou C, Theodoulou M, Yiallouras C, Damianou C. MRI guided focused ultrasound robotic system for the treatment of gynaecological tumors. *Int J Med Robot Comput Assist Surg*. 2016;12:46-52.
23. Yiannakou M, Menikou G, Yiallouras C, Ioannides C, Damianou C. MRI guided focused ultrasound robotic system for animal experiments. *Int J Med Robot Comput Assist Surg*. 2017;13(4):e1804. https://doi.org/10.1002/rcs.1804

How to cite this article: Antoniou A, Drakos T, Giannakou M, et al. Simple methods to test the accuracy of MRgFUS robotic systems. *Int J Med Robot*. 2021;17(4):e2287. https://doi.org/10.1002/rcs.2287